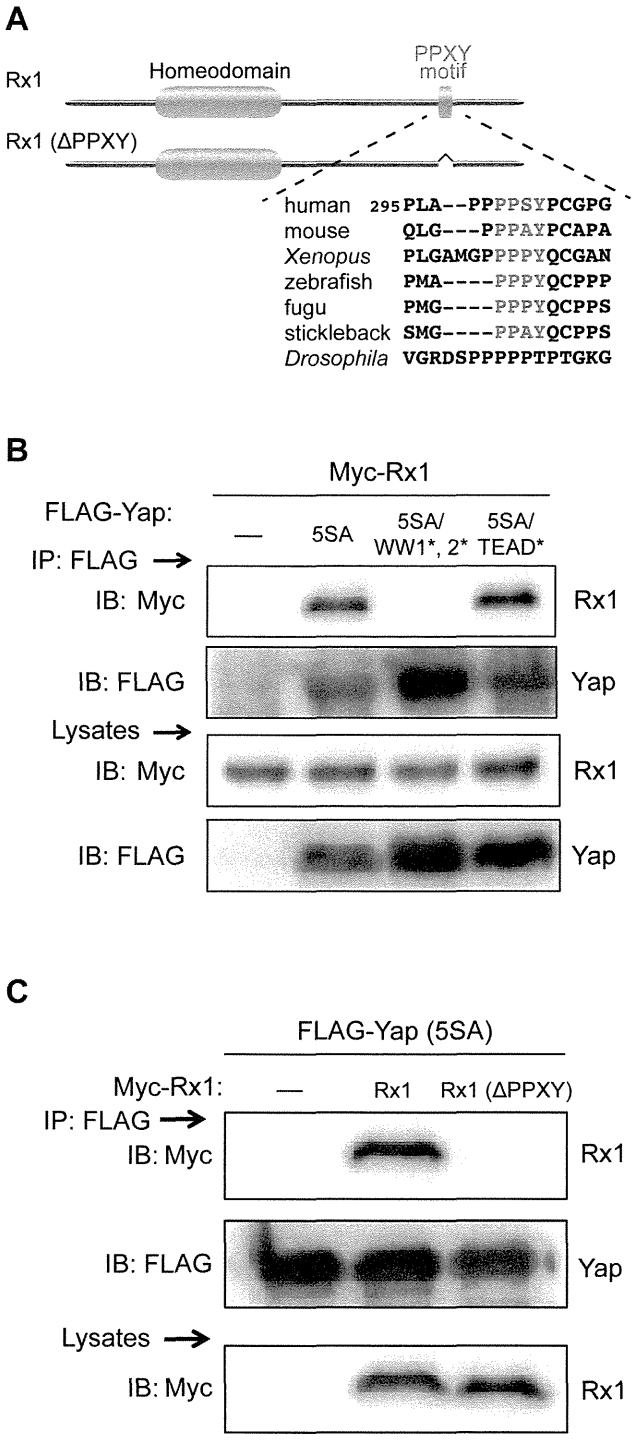

Figure 7. The WW domains of Yap interact with the PPXY motif of Rx1. (A) Schematic illustration of the zebrafish Rx1 and Rx1 (ΔPPXY) constructs. A partial amino acid sequence including the PPXY motif of zebrafish Rx1 was aligned with the sequences of Rx from the indicated species. The PPXY motif (red lettering) is highly conserved among vertebrates. A detailed alignment of Rx family proteins can be found in Fig. S5A. (B) Co-immunoprecipitation analysis of HEK293T cells transiently expressing Myc-Rx1 that were co-transfected with empty vector (–), or vector expressing Yap (5SA), Yap (5SA/WW1*, 2*) or Yap (5SA/TEAD*). Lysates were immunoprecipitated (IP) with anti-FLAG Ab to isolate Yap, followed by Western blotting (WB) with anti-Myc Ab to detect Myc-Rx1 (top), or with anti-FLAG Ab to detect FLAG-Yap (middle). (C) Co-immunoprecipitation analysis of HEK293T cells transiently expressing FLAG-Yap (5SA) that were co-transfected with empty vector (–), or vector expressing Rx1 or Rx1 (ΔPPXY). Lysates were IP'd using anti-FLAG Ab and subjected to WB with anti-Myc Ab to detect Rx1 (top), and with anti-FLAG Ab to detect Yap (middle). Bottom, WB analysis of total cell lysate using anti-Myc Ab to detect Rx1.
doi:10.1371/journal.pone.0097365.g007

Total RNA Extraction and RT-PCR Analysis

Total RNA was isolated from 7–10 zebrafish embryos at 2 dpf using TRIzol reagent according to the manufacturer's protocol (Invitrogen). First-strand cDNA was synthesized from 1 μg total RNA using SuperscriptIII reverse transcriptase (Invitrogen) and oligo-dT primer. Primers used for RT-PCR analysis of mRNA expression in zebrafish extracts were as follows: for *rhodopsin*, 5′-ACAGA GGGAC CGGCA TTCTA CG-3′ and 5′-CAGGC CATGA CCCAG GTGAA G-3′; for *crx*, 5′-AGAGA CGCGG CCGTC CCAAG-3′ and 5′-TCTTC ACGCA TCTTT CCTTC C-3′; for *otx5*, 5′-ACCCT AACAC TCCAC GGAAA C-3′ and 5′-TGCAG TCCAG GCCTG TAAAG-3′; for *otx2*, 5′-ATGAT GTCGT ATCTC AAGCA ACC-3′ and 5′-AGGAA GTGGA ACCAG CATAG CC-3′; for *rx1*, 5′-GATGC CGACA TGTTC TCCAA C-3′ and 5′-CGCCA TGGGC TGCAT GCTTT G-3′; for *rx2*, 5′-GGCTG CCTCT CCACA GAAAG-3′ and 5′-AAACC ACACC TGAAC TCGAA C-3′; for *β-actin*, 5′-CAGCT TCACC ACCAC AGC-3′ and 5′-GTGGA TACCG CAAGA TTCC-3′.

Plasmid Construction

Because our laboratory has been studying the small fish medaka for decades, we took advantage of the availability of medaka *yap (WT)* cDNA and the evolutionary conservation of *yap* sequences among fish species to create plasmids expressing mutated *yap* cDNAs. Our full-length medaka *yap (WT)* cDNA was originally isolated as a homolog of the human *YAP1-2β* isoform [19,44]. We subcloned this cDNA into a modified pCS2+ vector, which positions the FLAG tag at the N-terminus of the insert. The *Yap (5SA)* mutant and its variants with point mutations or deleted domains were generated by the inverse PCR-based method using the primers listed in Table S1. For heat shock experiments, *yap (WT)*, *yap (5SA)* and its variants were cloned into a modified pCS2+ vector in which the CMV promoter was replaced with the zebrafish *hsp70* promoter and the EGFP coding sequence (see Fig. 4A). For retina-specific expression, the zebrafish *hsp70* promoter was replaced with a 4-kb fragment of the medaka *rx3* promoter, which was isolated by PCR using the medaka genome and the primer pair 5′-CCGCC GGCCT CTGAT GTGAT GTTGA CAAA-3′ and 5′-CCCCA TGGTT GTCTA AAAAG GAACT TAAA-3′ (see Fig. 5A) [51]. For co-immunoprecipitation analyses, the PCR-amplified full-length zebrafish *rx1* cDNA was cloned into a pMyc-CMV5 vector (the kind gift of Dr. T. Katada, University of Tokyo), placing the Myc tag at the N-terminus of the insert. The *Rx1* variant in which the PPXY motif was deleted was generated by the inverse PCR-based method using the primers listed in Table S1.

Synthesis of Capped mRNA for Microinjection

Capped sense strand mRNA was synthesized using SP6 RNA polymerase and the mMESSAGE mMACHINE system (Ambion) according to the manufacturer's protocol. RNA injections were performed as described previously [52].

Microarray Analysis

TRIzol reagent was used to extract total RNA at 42, 48 or 54 hpf from whole zebrafish embryos that had been injected with *yap (WT)* or *yap (5SA)* mRNA. RNA quality assurance, cDNA

synthesis, and cRNA labeling and hybridization were carried out by Takara Bio Inc. (Otsu, Japan) using a Zebrafish (V3) Gene Expression Microarray 4X44K, the Low Input Quick Amp Labeling Kit, the Gene Expression Hybridization Kit, and the Gene Expression Wash Buffers Pack (all from Agilent Technologies) according to the manufacturer's protocols. Raw data extraction and analyses were performed using Agilent Feature Extraction software (Agilent Technologies). Gene Ontology analysis was conducted using KeyMolnet software (IMMD Inc., Tokyo, Japan).

Antibodies

Mouse monoclonal anti-FLAG (F1804) and rabbit polyclonal anti-Myc (C3956) antibodies (Abs) were purchased from Sigma–Aldrich Co.

Co-immunoprecipitation Assay

Co-immunoprecipitation assays were performed as previously described [53], with some modifications. HEK293T cells were plated in 10-cm dishes and transfected with the appropriate expression plasmids as described in the Figure Legends. Cells were washed twice with phosphate-buffered saline (PBS) and homogenized in binding buffer [150 mM NaCl, 1 mM EDTA, 0.5% Nonidet P-40, 1 mM EGTA, 5% glycerol, and 20 mM Tris-HCl (pH 7.4)] supplemented with 4 μg/mL aprotinin, 50 mM NaF, and 0.1 mM Na_3VO_4. Extracts were clarified by centrifugation for 10 min at 15,000g, and supernatants were precleared by incubation with 20 μl protein G-agarose beads (GE Healthcare) for 1 h at 4°C. After preclearing, supernatants were incubated with 20 μl anti-FLAG M2-agarose beads (Sigma–Aldrich) overnight at 4°C. The beads were washed three times with binding buffer, boiled in SDS sample buffer, and centrifuged. The supernatants were fractionated by SDS-PAGE and analyzed by Western blotting as described below.

Western Blotting

Immunoprecipitated materials and total cell extracts obtained as described above were fractionated by SDS-PAGE and transferred electrophoretically to PVDF membranes. Membranes were incubated in blocking solution [2% nonfat skim milk in Tris-buffered saline (TBS)] for 1 h at room temperature (RT). Blocked membranes were incubated with anti-FLAG or anti-Myc Ab in 5% BSA/TBS overnight at 4°C. Membranes were washed three times in 0.2% Tween 20 in TBS (TBST), incubated with anti-mouse/rabbit horseradish peroxidase-conjugated Abs in 2% nonfat skim milk in TBS for 1 h followed by three washes in TBST. Proteins were visualized using the SuperSignal West Femto Kit (Pierce) and a ChemiDoc XRS system (Bio-Rad), as described [52].

Supporting Information

Figure S1 Knockdown analysis of the zebrafish *mst2* gene. (A) Alignment of amino acid sequence of zebrafish Mst2 with its human and mouse homologs. Amino acids were aligned using the ClustalX program. Residues are colored according to their physicochemical properties [54]. Gaps have been introduced to optimize alignment. *, critical autophosphorylation site reflecting kinase activation [55]. Black underline, SARAH domain. Arrow, insertion site of the in-frame stop codon in the zebrafish *mst2* morphant. (B) Phylogenetic tree inferred from amino acid sequences of Mst proteins. Statistical significance (%) is shown on each node. Nodes with closed circles represent species divergences, while the node with the open circle represents gene duplication. Scale bar, 0.02 substitutions per site. (C) Top panel, schematic illustration of the target site of the *mst2* MO. Arrows indicate positions of primer pairs used in RT-PCR evaluation of MO efficacy. Bottom panel, partial sequences of native and intron 3-inserted *mst2* mRNAs. The stop codon (in red lettering) occurs in the inserted intron 3 of *mst2* mRNA, resulting in the production of a truncated Mst2 protein. (D) RT-PCR validation of *mst2* MO efficacy. Total RNA was extracted at 52 hpf from embryos injected with control MO (20 ng) or *mst2* MO (13.3 ng) and showing the phenotypes of abnormal eye pigmentation plus short body length (AP & SL), or abnormal eye morphology (AM) plus AP & SL. β-actin, loading control.
(TIF)

Figure S2 Morphological analysis of *yap (5SA)* mRNA-injected zebrafish embryos during the gastrulation and segmentation periods. (A) Alignment of amino acid sequence of medaka Yap with its zebrafish homolog performed as in Fig. S1. *, conserved serine residues phosphorylated by Lats. (B) Representative images of *yap (5SA) mRNA*-injected zebrafish embryos (N = 3) at the indicated developmental stages during gastrulation. Embryos were injected with EGFP mRNA as a control. (C) Representative lateral images of the embryos in (B) examined at the indicated stages during segmentation.
(TIF)

Figure S3 Reduced retinal gene expression in *mst2* morphants. (A) RT-PCR analysis of mRNA levels of the indicated retinal genes in zebrafish embryos injected with control MO or *mst2* MO and examined at 52 hpf. *Mst2* morphants were grouped by abnormal phenotype, as indicated. (B) RT-PCR analysis of *rhodopsin* mRNA expression in the morphants in (A). For A and B, results are representative of two independent trials.
(TIF)

Figure S4 A proposed model for the dual function of Hippo-Yap signaling during retinal progenitor cell proliferation versus photoreceptor cell differentiation. Left panel: When the Hippo pathway is inactive, activated Yap transactivates cell proliferation-related genes via association with TEAD. At the same time, activated Yap represses Rx1-mediated transcription of the *otx*, *crx* and *rhodopsin* genes, which results in suppression of photoreceptor cell differentiation. Right panel: When the Hippo pathway is active, Yap activation is blocked. TEAD on its own is insufficient to drive cell proliferation-related gene transcription. Without Yap-mediated suppression, Rx1-mediated transcription of *otx*, *crx* and *rhodopsin* is upregulated, leading to the differentiation of mature photoreceptor cells.
(TIF)

Figure S5 The PPXY motif in retinal transcription factors is highly conserved among vertebrate species. Sequence alignment of C-terminal amino acid residues of the retinal TFs Rx (A), ROR (B) and NRL (C) from the indicated species. Residues are colored according to their physicochemical properties. The red boxes indicate the positions of the PPXY motif. The blue boxes indicate the OAR domain of Rx (transactivation domain), the α-Helix10 domain of ROR, and the leucine zipper of NRL.
(TIF)

Table S1 List of primer sequences for plasmid constructions.
(TIF)

Methods S1 Supporting methods.
(DOC)

Acknowledgments

We thank numerous members of the Nishina laboratories for their helpful discussions and critical comments on the manuscript.

Author Contributions

Conceived and designed the experiments: YA SH MFS HN. Performed the experiments: YA SH MN. Analyzed the data: YA SH MN. Contributed reagents/materials/analysis tools: YA SH MN MFS HN. Wrote the paper: YA MFS HN.

References

1. Livesey FJ, Cepko CL (2001) Vertebrate neural cell-fate determination: lessons from the retina. Nat Rev Neurosci 2: 109–118.
2. Xiang M (2013) Intrinsic control of mammalian retinogenesis. Cell Mol Life Sci 70: 2519–2532.
3. Dowling JE (2012) The retina : an approachable part of the brain. Cambridge, Mass.: Belknap Press of Harvard University Press.: xvi, 355 p. p.
4. Swaroop A, Kim D, Forrest D (2010) Transcriptional regulation of photoreceptor development and homeostasis in the mammalian retina. Nat Rev Neurosci 11: 563–576.
5. Fadool JM, Dowling JE (2008) Zebrafish: a model system for the study of eye genetics. Prog Retin Eye Res 27: 89–110.
6. Stenkamp DL (2011) The rod photoreceptor lineage of teleost fish. Prog Retin Eye Res 30: 395–404.
7. Agathocleous M, Harris WA (2009) From progenitors to differentiated cells in the vertebrate retina. Annu Rev Cell Dev Biol 25: 45–69.
8. Jadhav AP, Mason HA, Cepko CL (2006) Notch 1 inhibits photoreceptor production in the developing mammalian retina. Development 133: 913–923.
9. Muranishi Y, Terada K, Inoue T, Katoh K, Tsujii T, et al. (2011) An essential role for RAX homeoprotein and NOTCH-HES signaling in Otx2 expression in embryonic retinal photoreceptor cell fate determination. J Neurosci 31: 16792–16807.
10. Yaron O, Farhy C, Marquardt T, Applebury M, Ashery-Padan R (2006) Notch1 functions to suppress cone-photoreceptor fate specification in the developing mouse retina. Development 133: 1367–1378.
11. Zhang H, Deo M, Thompson RC, Uhler MD, Turner DL (2012) Negative regulation of Yap during neuronal differentiation. Dev Biol 361: 103–115.
12. Pan D (2010) The hippo signaling pathway in development and cancer. Dev Cell 19: 491–505.
13. Zhao B, Tumaneng K, Guan KL (2011) The Hippo pathway in organ size control, tissue regeneration and stem cell self-renewal. Nat Cell Biol 13: 877–883.
14. Lin YT, Ding JY, Li MY, Yeh TS, Wang TW, et al. (2012) YAP regulates neuronal differentiation through Sonic hedgehog signaling pathway. Exp Cell Res 318: 1877–1888.
15. Hiemer SE, Varelas X (2013) Stem cell regulation by the Hippo pathway. Biochim Biophys Acta 1830: 2323–2334.
16. Lee JH, Kim TS, Yang TH, Koo BK, Oh SP, et al. (2008) A crucial role of WW45 in developing epithelial tissues in the mouse. EMBO J 27: 1231–1242.
17. Jiang Q, Liu D, Gong Y, Wang Y, Sun S, et al. (2009) yap is required for the development of brain, eyes, and neural crest in zebrafish. Biochem Biophys Res Commun 384: 114–119.
18. Hilman D, Gat U (2011) The evolutionary history of YAP and the hippo/YAP pathway. Mol Biol Evol 28: 2403–2417.
19. Hata S, Hirayama J, Kajiho H, Nakagawa K, Hata Y, et al. (2012) A novel acetylation cycle of transcription co-activator Yes-associated protein that is downstream of Hippo pathway is triggered in response to SN2 alkylating agents. J Biol Chem 287: 22089–22098.
20. Zhao B, Wei X, Li W, Udan RS, Yang Q, et al. (2007) Inactivation of YAP oncoprotein by the Hippo pathway is involved in cell contact inhibition and tissue growth control. Genes Dev 21: 2747–2761.
21. Gee ST, Milgram SL, Kramer KL, Conlon FL, Moody SA (2011) Yes-associated protein 65 (YAP) expands neural progenitors and regulates Pax3 expression in the neural plate border zone. PLoS One 6: e20309.
22. Shoji W, Sato-Maeda M (2008) Application of heat shock promoter in transgenic zebrafish. Dev Growth Differ 50: 401–406.
23. Cheng H, Khanna H, Oh EC, Hicks D, Mitton KP, et al. (2004) Photoreceptor-specific nuclear receptor NR2E3 functions as a transcriptional activator in rod photoreceptors. Hum Mol Genet 13: 1563–1575.
24. Furukawa T, Morrow EM, Cepko CL (1997) Crx, a novel otx-like homeobox gene, shows photoreceptor-specific expression and regulates photoreceptor differentiation. Cell 91: 531–541.
25. Whitaker SL, Knox BE (2004) Conserved transcriptional activators of the Xenopus rhodopsin gene. J Biol Chem 279: 49010–49018.
26. Pan Y, Martinez-De Luna RI, Lou CH, Nekkalapudi S, Kelly LE, et al. (2010) Regulation of photoreceptor gene expression by the retinal homeobox (Rx) gene product. Dev Biol 339: 494–506.
27. Nelson SM, Park L, Stenkamp DL (2009) Retinal homeobox 1 is required for retinal neurogenesis and photoreceptor differentiation in embryonic zebrafish. Dev Biol 328: 24–39.
28. Hu J, Sun S, Jiang Q, Sun S, Wang W, et al. (2013) Yes-associated protein (yap) is required for early embryonic development in zebrafish (danio rerio). Int J Biol Sci 9: 267–278.
29. Jukam D, Desplan C (2011) Binary regulation of Hippo pathway by Merlin/NF2, Kibra, Lgl, and Melted specifies and maintains postmitotic neuronal fate. Dev Cell 21: 874–887.
30. Nejigane S, Takahashi S, Haramoto Y, Michiue T, Asashima M (2013) Hippo signaling components, Mst1 and Mst2, act as a switch between self-renewal and differentiation in Xenopus hematopoietic and endothelial progenitors. Int J Dev Biol 57: 407–414.
31. Oh S, Lee D, Kim T, Kim TS, Oh HJ, et al. (2009) Crucial role for Mst1 and Mst2 kinases in early embryonic development of the mouse. Mol Cell Biol 29: 6309–6320.
32. Cao X, Pfaff SL, Gage FH (2008) YAP regulates neural progenitor cell number via the TEA domain transcription factor. Genes Dev 22: 3320–3334.
33. Basu S, Totty NF, Irwin MS, Sudol M, Downward J (2003) Akt phosphorylates the Yes-associated protein, YAP, to induce interaction with 14-3-3 and attenuation of p73-mediated apoptosis. Mol Cell 11: 11–23.
34. Komuro A, Nagai M, Navin NE, Sudol M (2003) WW domain-containing protein YAP associates with ErbB-4 and acts as a co-transcriptional activator for the carboxyl-terminal fragment of ErbB-4 that translocates to the nucleus. J Biol Chem 278: 33334–33341.
35. Yagi R, Chen LF, Shigesada K, Murakami Y, Ito Y (1999) A WW domain-containing yes-associated protein (YAP) is a novel transcriptional co-activator. EMBO J 18: 2551–2562.
36. Zaidi SK, Sullivan AJ, Medina R, Ito Y, van Wijnen AJ, et al. (2004) Tyrosine phosphorylation controls Runx2-mediated subnuclear targeting of YAP to repress transcription. EMBO J 23: 790–799.
37. Bork P, Sudol M (1994) The WW domain: a signalling site in dystrophin? Trends Biochem Sci 19: 531–533.
38. Chen HI, Sudol M (1995) The WW domain of Yes-associated protein binds a proline-rich ligand that differs from the consensus established for Src homology 3-binding modules. Proc Natl Acad Sci U S A 92: 7819–7823.
39. Sudol M, Harvey KF (2010) Modularity in the Hippo signaling pathway. Trends Biochem Sci 35: 627–633.
40. Fujieda H, Bremner R, Mears AJ, Sasaki H (2009) Retinoic acid receptor-related orphan receptor alpha regulates a subset of cone genes during mouse retinal development. J Neurochem 108: 91–101.
41. Jia L, Oh EC, Ng L, Srinivas M, Brooks M, et al. (2009) Retinoid-related orphan nuclear receptor RORbeta is an early-acting factor in rod photoreceptor development. Proc Natl Acad Sci U S A 106: 17534–17539.
42. Srinivas M, Ng L, Liu H, Jia L, Forrest D (2006) Activation of the blue opsin gene in cone photoreceptor development by retinoid-related orphan receptor beta. Mol Endocrinol 20: 1728–1741.
43. Pobbati AV, Hong W (2013) Emerging roles of TEAD transcription factors and its coactivators in cancers. Cancer Biol Ther 14: 390–398.
44. Gaffney CJ, Oka T, Mazack V, Hilman D, Gat U, et al. (2012) Identification, basic characterization and evolutionary analysis of differentially spliced mRNA isoforms of human YAP1 gene. Gene 509: 215–222.
45. Webb C, Upadhyay A, Giuntini F, Eggleston I, Furutani-Seiki M, et al. (2011) Structural features and ligand binding properties of tandem WW domains from YAP and TAZ, nuclear effectors of the Hippo pathway. Biochemistry 50: 3300–3309.
46. Pellissier LP, Alves CH, Quinn PM, Vos RM, Tanimoto N, et al. (2013) Targeted ablation of crb1 and crb2 in retinal progenitor cells mimics leber congenital amaurosis. PLoS Genet 9: e1003976.
47. Yu FX, Guan KL (2013) The Hippo pathway: regulators and regulations. Genes Dev 27: 355–371.
48. Westerfield M (1994) The Zebrafish Book: A Guide for the Laboratory Use of Zebrafish (Branchydanio rerio): Institute of Neuroscience. Eugene, OR: University of Oregon.
49. Kimmel CB, Ballard WW, Kimmel SR, Ullmann B, Schilling TF (1995) Stages of embryonic development of the zebrafish. Dev Dyn 203: 253–310.
50. Saitou N, Nei M (1987) The neighbor-joining method: a new method for reconstructing phylogenetic trees. Mol Biol Evol 4: 406–425.
51. Rembold M, Loosli F, Adams RJ, Wittbrodt J (2006) Individual cell migration serves as the driving force for optic vesicle evagination. Science 313: 1130–1134.
52. Seo J, Asaoka Y, Nagai Y, Hirayama J, Yamasaki T, et al. (2010) Negative regulation of wnt11 expression by Jnk signaling during zebrafish gastrulation. J Cell Biochem 110: 1022–1037.
53. Shimomura T, Miyamura N, Hata S, Miura R, Hirayama J, et al. (2014) The PDZ-binding motif of Yes-associated protein is required for its co-activation of TEAD-mediated CTGF transcription and oncogenic cell transforming activity. Biochem Biophys Res Commun 443: 917–923.
54. Gouy M, Guindon S, Gascuel O (2010) SeaView version 4: A multiplatform graphical user interface for sequence alignment and phylogenetic tree building. Mol Biol Evol 27: 221–224.
55. Praskova M, Khoklatchev A, Ortiz-Vega S, Avruch J (2004) Regulation of the MST1 kinase by autophosphorylation, by the growth inhibitory proteins, RASSF1 and NORE1, and by Ras. Biochem J 381: 453–462.

Biochemical and Biophysical Research Communications 457 (2015) 493–499

Contents lists available at ScienceDirect

Biochemical and Biophysical Research Communications

journal homepage: www.elsevier.com/locate/ybbrc

Extracellular acidification activates ovarian cancer G-protein-coupled receptor 1 and GPR4 homologs of zebra fish

Yuta Mochimaru [a], Morio Azuma [b], Natsuki Oshima [a], Yuta Ichijo [a], Kazuhiro Satou [a], Kouhei Matsuda [b], Yoichi Asaoka [c], Hiroshi Nishina [c], Takashi Nakakura [d], Chihiro Mogi [e], Koichi Sato [e], Fumikazu Okajima [e], Hideaki Tomura [a, *]

[a] Laboratory of Cell Signaling Regulation, Department of Life Sciences, School of Agriculture, Meiji University, Kawasaki 214-8571, Japan
[b] Laboratory of Regulatory Biology, Graduate School of Science and Engineering, University of Toyama, 3190 Gofuku, Toyama 930-8555, Japan
[c] Department of Developmental and Regenerative Biology, Medical Research Institute, Tokyo Medical and Dental University, Tokyo 113-8510, Japan
[d] Department of Anatomy, Graduate School of Medicine, Teikyo University, 2-11-1 Kaga Itabashi-Ku, Tokyo 173-8605, Japan
[e] Laboratory of Signal Transduction, Institute for Molecular and Cellular Regulation, Gunma University, Maebashi 371-8512, Japan

ARTICLE INFO

Article history:
Received 12 December 2014
Available online 7 January 2015

Keywords:
Zebra fish
OGR1
GPR4
Proton sensing

ABSTRACT

Mammalian ovarian G-protein-coupled receptor 1 (OGR1) and GPR4 are identified as a proton-sensing G-protein-coupled receptor coupling to multiple intracellular signaling pathways. In the present study, we examined whether zebra fish OGR1 and GPR4 homologs (zOGR1 and zGPR4) could sense protons and activate the multiple intracellular signaling pathways and, if so, whether the similar positions of histidine residue, which is critical for sensing protons in mammalian OGR and GPR4, also play a role to sense protons and activate the multiple signaling pathways in the zebra fish receptors. We found that extracellular acidic pH stimulated CRE-, SRE-, and NFAT-promoter activities in zOGR1 overexpressed cells and stimulated CRE- and SRE- but not NFAT-promoter activities in zGPR4 overexpressed cells. The substitution of histidine residues at the 12th, 15th, 162th, and 264th positions from the N-terminal of zOGR1 with phenylalanine attenuated the proton-induced SRE-promoter activities. The mutation of the histidine residue at the 78th but not the 84th position from the N-terminal of zGPR4 to phenylalanine attenuated the proton-induced SRE-promoter activities. These results suggest that zOGR1 and zGPR4 are also proton-sensing G-protein-coupled receptors, and the receptor activation mechanisms may be similar to those of the mammalian receptors.

1. Introduction

Mammalian ovarian cancer G-protein-coupled receptor 1 (OGR1) and GPR4 were originally reported to be activated by lysolipids, such as sphingosylphosphorylcholine (SPC) and lysophosphatidylcholine (LPC), which act as ligands [1]; however, the direct binding of the lipids to the receptors has not been proven. On the other hand, Ludwig reported that the human receptors sense extracellular protons and activate intracellular signaling pathways through trimeric G proteins [2]. Thus, human OGR1 stimulation causes phospholipase C (PLC) activation and subsequent intracellular Ca^{2+} ($[Ca^{2+}]_i$) mobilization through $G_{q/11}$ proteins, and human GPR4 stimulates adenylyl cyclase activation through G_s proteins, in response to the extracellular acidification. Later, we showed that human OGR1 is also coupled to G_s/cAMP and G_{13}/Rho signaling pathways [3,4], and GPR4 is coupled to G_{13}/Rho and $G_{q/11}$/PLC signaling pathways [4,5], when the receptors were overexpressed in HEK293T cells. Site mutagenesis studies show that the specific histidine residues at the extracellular surface of the receptors are responsible for proton sensing [2,5].

OGR1 and GPR4 expressions are widely detected in many tissues [1]. The receptor expressions are also reported in vascular endothelial and smooth muscle cells [6–19]. Under an acidic pH condition, OGR1 mediates COX-2, MKP-1, IL-6, CTGF, VCAM-1, and ICAM-1 expressions and PGI_2 production in human vascular smooth muscle and airway smooth muscle cells [15–19]. GPR4 mediates VCAM-1, ICAM-1, COX-2, and a number of inflammatory gene expressions [9,10]. The physiological and pathophysiological

Abbreviations: [1]z, zebra fish (*Danio rerio*); OGR1, ovarian cancer G-protein-coupled receptor 1; GPCR, G-protein-coupled receptor.

* Corresponding author. Fax: +81 44 934 7825.
E-mail address: tomurah@meiji.ac.jp (H. Tomura).

http://dx.doi.org/10.1016/j.bbrc.2014.12.105
0006-291X/

roles of OGR1 and GPR4 are examined using OGR1-and GPR4-deficient mice. However, the molecular mechanism by which the receptors are concerned with the phenotype is largely unknown.

Zebra fish can provide a useful vertebrate model system to elucidate the molecular mechanism of the receptor functions in vivo. The embryo is transparent, and development takes place outside the maternal body. These characteristics make them suitable to use for in vivo imaging. Indeed, zebra fish have been used in especially studies of blood vessel formation [20] and cancer invasion [21].

We found zebra fish OGR1 and GPR4 homologs (zOGR1 and zGPR4) in the genome database; however, their characterizations have not yet been reported. In this study, we characterized the functions of the homologs and focused on their ligand specificity and signaling pathways by expressing them in HEK293T cells. We found that these receptors sense protons like the mammalian receptors and activate multiple signaling pathways.

2. Materials and methods

2.1. Materials

A dual luciferase kit was purchased from Promega (Tokyo, Japan); Fura2 AM from Dojindo (Tokyo, Japan); fatty acid-free BSA from Calbiochem-Novabiochem Co. (San Diego, CA); and Lipofectamine 2000 Reagent from Life Technologies (Tokyo, Japan). The sources of all other reagents were the same as described previously [4,5].

2.2. Preparation of receptor cDNA plasmids and expression

The entire coding regions of zOGR1 (1032 bp, GenBank accession No. XM_001339552), zGPR4 (1122 bp, GenBank accession No. XM_687123), zOGR1-H4F (the 12th, 15th, 162th, and 264th positions of histidine from the N terminus were substituted with phenylalanine), GPR4-H78F (the 78th position of histidine from the N terminus was substituted with phenylalanine), and GPR4-H84F (the 84th position of histidine from the N terminus was substituted with phenylalanine) were synthesized and cloned into a pBo-CMV vector (Takara, Japan) with a Kozak sequence (CCACC) in front of the 1st methionine codon.

The wild-type or the substituted constructs were transfected into HEK293T cells using Lipofectamine 2000 Reagent (Invitrogen, Carlsbad, CA) and plated onto 12 multiplates, as described previously [4].

2.3. Cell cultures

HEK293T cells were provided by the RIKEN BRC through the National Bio-Resource Project of the MEXT, Japan. The cells were cultured in DMEM containing 10% (v/v) FBS (Life Technologies) in a humidified air/CO_2 (19:1) atmosphere.

2.4. Measurement of intracellular calcium

The change in intracellular Ca^{2+} concentration ($[Ca^{2+}]_i$) was measured using a fura-2 method as described previously [22,23]. The changes in the intensities of 540 nm fluorescence obtained by 340 nm and 380 nm excitations were monitored by an FP-8200 spectrofluorometer (JASCO, Tokyo, Japan).

2.5. Dual luciferase reporter assay

cAMP response element (CRE)-, serum response element (SRE)-, or nuclear factor of activated T-cells (NFAT)-driven promoter activity was assayed using the PathDetect Signal Transduction Pathway cis-Reporting Systems (Agilent Technologies, Santa Clara, CA) as described in the previous paper [4].

2.6. Reverse transcriptase (RT) polymerase chain reaction (PCR)

Total RNA was extracted from each 10 embryos or baby fishes at 3, 24, 48, 72, and 96 h post fertilization (hpf). RT-PCR was carried out as follows: preheat at 95 °C for 4 min, then proceed to 34 cycles (OGR1 and GPR4) or 30 cycles (β-actin) at 94 °C for 30 s, 62 °C for 30 s, and 72 °C for 30 s. The forward primers were CGGGACTG-CAACTTCATTGAG for zOGR1, GAAGTGAGACCATGTGCAAC for zGPR4, and GTGATGGACTCTGGTGATGGTGT for zβ-actin. The reverse primers were AGTGGAGTGTGTGTTGAACCTTC for zOGR1, AGAGGTCTGCTATCGAGAGGTTC for zGPR4, and TGAAGCTG-TAGCCTCTCTCGGTC for zβ-actin. The expected size of each product was 204 bp for zOGR1, 201 bp for zGPR4, and 148 bp for zβ-actin.

2.7. Data presentation

All the experiments were performed in duplicate or triplicate. The results of multiple observations are presented as the mean ± SE from more than three different batches of cells unless otherwise stated. Statistical significance was assessed by ANOVA; values were considered significant at $p < 0.05$ (*).

3. Results

3.1. Zebra fish OGR1 and GPR4 homologs sense protons to activate multiple signaling pathways

Transient expression of wild-type zebra fish OGR1 (zOGR1) and GPR4 (zGPR4) homologs in HEK293T cells induced CRE-, SRE-, and NFAT-driven transcriptional activation when the extracellular pH was reduced from 7.6 to 6.3, indicating that these homologs sense protons to activate multiple signaling pathways (Fig. 1A, B). The activated signaling pathways were different between zOGR1 and zGPR4: zOGR1 activates all three (CRE, SRE, and NFAT) pathways. On the other hand, zGPR4 activates CRE and SRE pathways but not the NFAT pathway.

In the previous study [4], we showed that CRE, SRE, and NFAT promoters were activated through the G_s-protein/adenylyl cyclase/cAMP signaling pathway, $G_{12/13}$-protein/Rho signaling pathway, and G_q-protein/phospholipase C–Ca^{2+} signaling pathway in HEK293T cells, respectively. In agreement with this, the $[Ca^{2+}]_i$ was increased, which reflects phospholipase C activation when extracellular pH was reduced from 7.6 to 6.3 in the zOGR1 expressed cells (Fig. 1C). On the other hand, the $[Ca^{2+}]_i$ concentration in the zGPR4 expressed cells was not significantly increased from that in vector-transfected HEK293 cells at pH 6.3 (Fig. 1C). The significant activation of CRE and SRE promoters was observed in the zOGR1 and zGPR4 expressed cells, even at a neutral pH of 7.4 (Fig. 1A, B). Thus, zOGR1 and zGPR4 are stimulated under neutral pH as if the receptors had constitutive activity.

3.2. The similar position of histidine residue in zOGR1 and zGPR4 to that of human receptors is involved in the receptor activation

The histidine residues in the extracellular surface of human OGR1 and GPR4 are crucial for sensing protons [2,5]. The amino acid identity between human and zebra fish OGR1 is 57%, and that between human and zebra fish GPR4 is 73%. The four residues of the five crucial histidine residues (depicted as H in bold type in Fig. 2A) to sense protons in human OGR1 are conserved in zOGR1. To clarify that the histidine residues of zOGR1 play a role to sense protons, we made a construct in which the four histidine residues of the 12th,

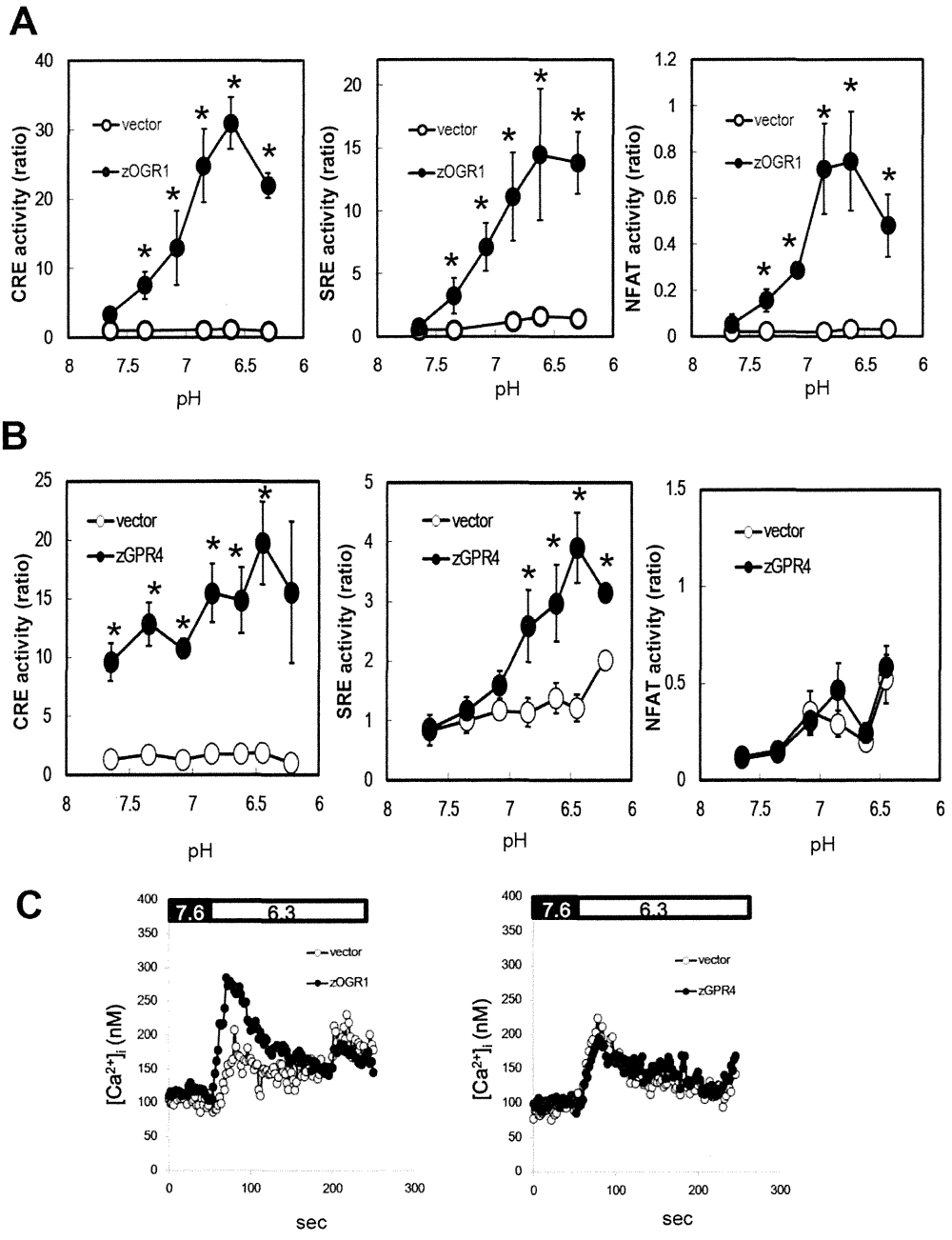

Fig. 1. Extracellular acidic pH-induced CRE-, SRE-, and NFAT-driven transcriptional activation (A, B) and an increment of $[Ca^{2+}]_i$ (C) in zOGR1-and zGPR4-transfected HEK293T cells. In A and B, HEK293T cells were transiently transfected with wild-type zOGR1 and zGPR4 (closed circle) expression plasmids and a pBo-CMV vector (open circle) together with pRL-TK and pCRE-, pSRE-, or pNFAT-luc. The cells were incubated for 6 h at the indicated pH to measure CRE-, SRE-, and NFAT-promoter activities. See "Materials and methods" for more detail. Results are means ± SE. The asterisk (*) indicates that the effects of zOGR1 and zGPR4 were significant under the indicated pH. In C, the cells were harvested from the dishes, and $[Ca^{2+}]_i$ was measured. The typical trace of $[Ca^{2+}]_i$ change by acidic pH (pH 6.3) was shown in the vector-(open circle), zOGR1-, and zGPR4-(closed circle) transfected cells. Two other experiments yielded similar results.

15th, 162th, and 264th positions from the N terminus of zOGR1 were substituted with phenylalanine (H4F) and examined the SRE-promoter activities upon reducing extracellular pH from 7.6 to 6.3. As shown in the left panel of Fig. 2C, the mutant showed little activity. Thus, the histidine residues, which are crucial for sensing protons in human OGR1, are conserved in zOGR1. Next we examined whether the similar position of histidine residue is responsible for proton sensing. Based on the result of human GPR4 [5], the histidine residue of the 78th amino acid from the N terminus of zGPR4 is supposed to play a role to sense protons. On the other hand, the histidine residue of the 84th amino acid may be not to play that role. We made two different mutants in which the histidine residues at the 78th and 84th positions were substituted with phenylalanine (H78F and H84F, respectively) and examined their activity. As expected, the H78F mutant showed reduced SRE-promoter activity compared with the activity of wild-type zGPR4; however, the activity of the H84F mutant was comparable to the activity of the wild type (Fig. 2C, right panel). This suggests that the histidine position for proton sensing is conserved between the human and zebra fish receptors.

A

```
H.sapiens       MGNITADNSSMSCTIDHTIHQTLAPVVYVTVLVVGFPANCLSLYFGYLQIKARNELGVYL 60
D.rerio         -----MSEEQINCTINHDIHQYLFSVAYLLVLLVGLPANAYSLYHAWLQLKARNELGVYL 55

H.sapiens       CNLTVADLFYICSLPFWLQYVLQHDNWSHGDLSCQVCGILLYENIYISVGFLCCISVDRY 120
D.rerio         LNLTISDLLYLGSLPLWLQYIFQGDNWSGSEWLCQLCGFLLYENIYVSIGFLCCISIDRY 115

H.sapiens       LAVAHPFRFHQFRTLKAAVGVSVVIWAKELLTSIYFLMHEEVIEDENQHRVCFEHYPIQA 180
D.rerio         LAVVYPFRFSAFRTVRAATLVSTVVWLKELAVGVVFFLHKELSRDKHNQSVCFEHYPMKT 175

H.sapiens       WQRAINYYRFLVGFLFPICLLLASYQGILRAVRRSHGTQKSRKDQIQRLVLSTVVIFLAC 240
D.rerio         WEYQINYYRFYIGFLFPLGILSVSYFRVLRAVGKSAGTQTSQKIRIKYLVTSTIVIFLVC 235

H.sapiens       FLPYHVLLLVRSVWEASCDFAKGVFNAYHFSLLLTSFNCVADPVLYCFVSETTHRDLARL 300
D.rerio         FSPYHIFLLVRTIFERDCNFIESIFNYYHFSLLLTSFNCVADPALYCFISESAQKGIQKA 295

H.sapiens       RGACLAFLTCSRTGRAREAYPLGAPEASGKSGAQGEEPELLTKLHPAFQTPNSPGSGGFP 360
D.rerio         HDACTRVFCCCSKSHGRFNTHSTELAVTNDNVTGTSVVTLLQQIKTEV---------- 343

H.sapiens       TGRLA 365
D.rerio         -----
```

B

```
H.sapiens       ---------MGNHTWEGCHVDSRVDHLFPPSLYIFVIGVGLPTNCLALWAAYRQVQQRNE 51
D.rerio         MASLRGSETMCNITTS-CNVDSNIDQFFQPTLYIIVIVLGFPTNCMALWAAYMQVKQKNE 59

H.sapiens       LGVYLMNLSIADLLYICTLPLWVDYFLHHDNWIHGPGSCKLFGFIFYTNIYISIAFLCCI 111
D.rerio         LGIYLMNLSIADLLYITTLPLWIDYFVHHDNWIHGQVSCKLFGFIFYTNIYVSIAFLCCI 119
                                            78    84

H.sapiens       SVDRYLAVAHPLRFARLRRVKTAVAVSSVVWATELGANSAPLFHDELFRDRYNHTFCFEK 171
D.rerio         SVDRYLAVAHPLKFAKVRRVKTALLVSAIVWLTEIVANSAPLFHDELFQDRFNHTFCFEK 179

H.sapiens       FPMEGWVAWMNLYRVFVGFLFPWALMLLSYRGILRAVRGSVSTERQEKAKIKRLALSLIA 231
D.rerio         YPMEPWVAGMNLYRTFLGFLAPWGIMLAAYRGILRAVRGNVSTERQEKAKIKRLALSLIL 239

H.sapiens       IVLVCFAPYHVLLLSRSAIYLGRPWDCGFEERVFSAYHSSLAFTSLNCVADPILYCLVNE 291
D.rerio         IVLLCFAPYHVLLLWRSVLFLINPCDCGGEENLFGAYHVTLALTSLNCVADPILYCFVNE 299

H.sapiens       GARSDVAKALHNLLRFLASDK-PQEMANASLTLETPLTSKR-NSTAKAMTGSWAATPPSQ 349
D.rerio         GARHDVGRALATLLGLFQRGKSPETLMGASITVETPLAVKKPDFYSEVKTNAYKNDIEVL 359

H.sapiens       GDQ-VQLKMLPPAQ 362
D.rerio         KDECLQMTILSVKK 373
```

C

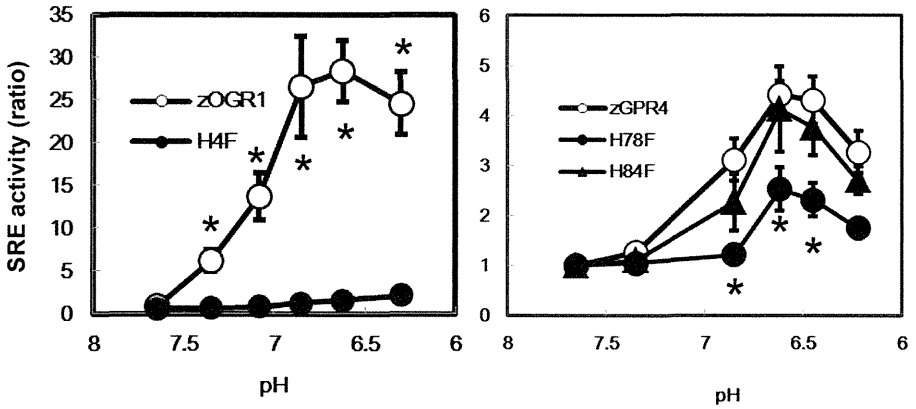

Fig. 2. Amino acid sequence alignment between OGR1 (A) and GPR4 (B) of humans (H.sapiens) and zebra fish (*D. rerio*) and the effects of the substitution of histidine with phenylalanine in zOGR1 and zGPR4 on proton-induced SRE-promoter activity (C). The histidine (H), which is concerned with the proton sensing of human OGR1 and GPR4, is depicted in bold type. All the corresponding histidines of zOGR1 were substituted with phenylalanine (H4F). The number in B indicates the mutant, whose histidine was substituted with phenylalanine in zGPR4 (H78F or H84F). HEK293T cells were transiently transfected with wild-type zOGR1, zGPR4 together with pRL-TK, and pSRE-luc. The cells were incubated for 6 h at the indicated pH to measure SRE-promoter activity. Results are means ± SE. The asterisk (*) indicates that the activities of H4F and H78F were significantly different from those of the wild-type receptors under the indicated pH.

3.3. LPC and SPC do not seem to mediate SRE activation in the zOGR1 and zGPR4 overexpressed cells

LPC and SPC modulate the mammalian OGR1-and GPR4-mediated cell responses [3,6,11,24–28]. We next examined whether these lysolipids modulate the zOGR1-and/or GPR4-mediated SRE-promoter activation. As shown in the right panels of Fig. 3A and B, SPC at 10 μM induced SRE-promoter activation; however, similar activation was also detected in the vector-transfected cells. Thus, SPC does not modulate zOGR1-and zGPR4-mediated SRE-reporter activation. LPC at 10 μM did not stimulate SRE-promoter activation (Fig. 3A and B, left panels).

3.4. zOGR1 and zGPR4 were expressed in zebra fish

We finally examined the gene expression of zOGR1 and zGPR4 at different developmental stages of zebra fish embryogenesis (Fig. 4). Both receptors were expressed in zebra fish; however, the expression pattern was different, i.e., the transcript of zOGR1 was detected in the stages from 24 to 96 hpf. On the other hand, the transcript of zGPR4 was present in all the analyzed stages from 3 to 96 hpf.

4. Discussion

In the present study, we show for the first time that OGR1 and GPR4 homologs of zebra fish sensed protons and activated the multiple signaling pathways (Fig. 1A and B). Thus, zOGR1 and zGPR4 are proton-sensing GPCRs, as are human OGR1 and GPR4; however, the NFAT-reporter activation profile was different between zebra fish and human GPR4. In the previous study [4,5], extracellular acidification induced NFAT-driven transcriptional activity of human GPR4; however, the transcriptional activity of zGPR4 was not attenuated at any pH tested (Fig. 1B). It may be due to a difference of coupling efficiency to human $G_{q/11}$ between human and zebra fish GPR4. It should be investigated in the future. The high CRE-reporter activation of zGPR4 was detected even at pH 7.6 and was further enhanced by extracellular acidification (Fig. 1B). The increment of cAMP accumulation is also detected even at pH 7.6 in the original report [2]. This is not due to the effect of overexpression of GPR4. The high cAMP accumulation at pH 7.8 is reported in the kidney cells [29].

The specific histidine residues of human OGR1 and GPR4 play a crucial role in sensing extracellular protons [2,5,30]. Five histidine residues (depicted as H in bold type in Fig. 2A) are responsible for sensing and activating the signaling pathways in human OGR1 [14,31]. Four of the five corresponding positions of histidine residues are conserved in zOGR1 (Fig. 2A). In this study, the mutant that was substituted in these four histidine residues with phenylalanine failed to stimulate the SRE-reporter (Fig. 2C, left panel). This result suggests that the activation mechanisms are similar between human and zebra fish OGR1. We confirmed the similarity of the receptor activation between human and zebra fish using the zGPR4 mutants (Fig. 2B). As shown in Fig. 2C, the mutant of the 78th but not of 84th position attenuated acidic pH-induced SRE-reporter activation. This result is the same as the result of human GPR4 [5]. The similarity between the human and zebra fish receptors

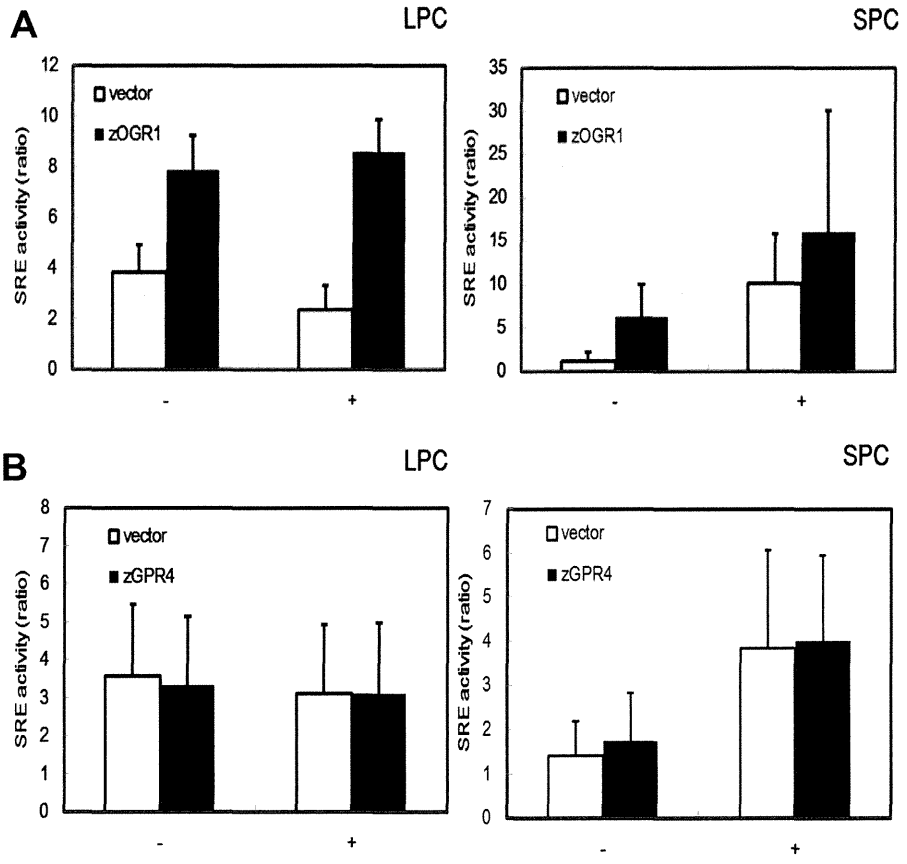

Fig. 3. Effect of SPC and LPC on SRE-promoter activity in zOGR1 (A) and zGPR4 (B) overexpressed HEK292T cells. HEK293T cells were transiently transfected with wild-type zOGR1 and with zGPR4 together with pRL-TK and pSRE-luc. The cells were incubated for 6 h in the presence (+) or absence (−) of 10 μM LPC or 10 μM SPC to measure SRE-promoter activity. Results are means ± SE of six determinations from two separate experiments.

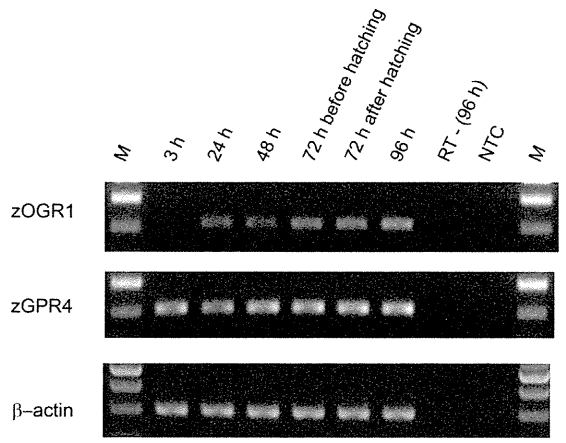

Fig. 4. Expression pattern of zOGR1 or zGPR4 transcripts during zebra fish embryogenesis. RT-PCR reactions were performed at different stages of embryogenesis. The developmental stage was depicted as hours post fertilization (h) on top of the figure. β-actin was used as a control of RT-PCR. RT-indicates a negative PCR control reaction without reverse transcriptase reaction. NTC also indicates a negative control reaction without RNA. M indicates a 100 bp molecular weight marker. The expected size of zOGR1 is 204 bp, and that of zGPR4 is 201 bp.

suggests that we can use zebra fish for the screening of chemical compounds that will have agonist and/or antagonist activity with human OGR1 and GPR4.

Human OGR1 and GPR4 were originally reported as the receptors for SPC and LPC; however, the report was retracted. In this study, we examined the possibility of whether these lysolipids stimulate the zOGR1-and zGPR4-mediated pathways. As shown in Fig. 3, LPC did not stimulate the zOGR1-or zGPR4-induced reporter activity. On the other hand, SPC stimulated SRE-promoter activation; however, similar activation was also detected in vector-transfected cells. This zOGR1-and zGPR4-independent SPC action may be partly mediated by endogeneous S1P receptors [4].

zOGR1 and zGPR4 were expressed in various developmental stages of zebra fish (Fig. 4). These receptors may play physiological and pathophysiological common roles in vertebrates. The physiological and pathophysiological roles of OGR1 and GPR4 have been examined using OGR1-and GPR4-deficient mice. OGR1-deficient mice show tumor growth inhibition [32], enhanced proton extrusion in the proximal tube of the kidney [14], and decreased insulin secretion from the islet [33]. GPR4-deficient mice show vascular abnormality [12], reduced angiogenesis and tumor growth [34], decreased acid secretion from the kidney [29], and improved glucose tolerance and insulin sensitivity [35]. However, the molecular mechanism by which the receptors are concerned with the phenotype is largely unknown.

Zebra fish have been extensively used for in vivo imaging, especially in the studies of blood vessel formation [20] and cancer invasion [21]. Since OGR1-and GPR4-deficient mice show the receptors' effect on tumor growth and vascular formation, as described above, zebra fish studies will provide useful information for the physiological and pathophysiological roles of OGR1 and GPR4 in the future.

Disclosure statement

The authors have declared no conflicts of interest.

Acknowledgments

This work was supported by Grants-in-Aid (C) for Scientific Research from the Japan Society for the Promotion of Science Grant Number 24580436 and the MEXT-Supported Program for the Strategic Research Foundation at Private Universities, 2014–2018.

References

[1] Y. Xu, Sphingosylphosphorylcholine and lysophosphatidylcholine: G protein-coupled receptors and receptor-mediated signal transduction, Biochim. Biophys. Acta 1582 (2002) 81–88.
[2] M.G. Ludwig, M. Vanek, D. Guerini, J.A. Gasser, C.E. Jones, U. Junker, H. Hofstetter, R.M. Wolf, K. Seuwen, Proton-sensing G-protein-coupled receptors, Nature 425 (2003) 93–98.
[3] C. Mogi, H. Tomura, M. Tobo, J.Q. Wang, A. Damirin, J. Kon, M. Komachi, K. Hashimoto, K. Sato, F. Okajima, Sphingosylphosphorylcholine antagonizes proton-sensing ovarian cancer G-protein-coupled receptor 1 (OGR1)-mediated inositol phosphate production and cAMP accumulation, J. Pharmacol. Sci. 99 (2005) 160–167.
[4] M. Tobo, H. Tomura, C. Mogi, J.Q. Wang, J.P. Liu, M. Komachi, A. Damirin, T. Kimura, N. Murata, H. Kurose, K. Sato, F. Okajima, Previously postulated "ligand-independent" signaling of GPR4 is mediated through proton-sensing mechanisms, Cell. Signal. 19 (2007) 1745–1753.
[5] J.P. Liu, T. Nakakura, H. Tomura, M. Tobo, C. Mogi, J.Q. Wang, X.D. He, M. Takano, A. Damirin, M. Komachi, K. Sato, F. Okajima, Each one of certain histidine residues in G-protein-coupled receptor GPR4 is critical for extracellular proton-induced stimulation of multiple G-protein-signaling pathways, Pharmacol. Res. 61 (2010) 499–505.
[6] K.S. Kim, J. Ren, Y. Jiang, Q. Ebrahem, R. Tipps, K. Cristina, Y.J. Xiao, J. Qiao, K.L. Taylor, H. Lum, B. Anand-Apte, Y. Xu, GPR4 plays a critical role in endothelial cell function and mediates the effects of sphingosylphosphorylcholine, Faseb J. 19 (2005) 819–821.
[7] B. Dong, H. Zhou, C. Han, J. Yao, L. Xu, M. Zhang, Y. Fu, Q. Xia, Ischemia/Reperfusion-induced CHOP expression promotes apoptosis and impairs renal function recovery: the role of acidosis and GPR4, PLoS One 9 (2014) e110944.
[8] J. Ren, W. Jin, Y.E. Gao, Y. Zhang, X. Zhang, D. Zhao, H. Ma, Z. Li, J. Wang, L. Xiao, R. Liu, Y. Chen, J. Qian, L. Niu, H. Wei, Y. Liu, Relations between GPR4 expression, microvascular density (MVD) and clinical pathological characteristics of patients with epithelial ovarian carcinoma (EOC), Curr. Pharm. Des. 20 (2014) 1904–1916.
[9] L. Dong, Z. Li, N.R. Leffler, A.S. Asch, J.T. Chi, L.V. Yang, Acidosis activation of the proton-sensing GPR4 receptor stimulates vascular endothelial cell inflammatory responses revealed by transcriptome analysis, PLoS One 8 (2013) e61991.
[10] A. Chen, L. Dong, N.R. Leffler, A.S. Asch, O.N. Witte, L.V. Yang, Activation of GPR4 by acidosis increases endothelial cell adhesion through the cAMP/Epac pathway, PLoS One 6 (2011) e27586.
[11] F. Huang, D. Mehta, S. Predescu, K.S. Kim, H. Lum, A novel lysophospholipid- and pH-sensitive receptor, GPR4, in brain endothelial cells regulates monocyte transmigration, Endothelium 14 (2007) 25–34.
[12] L.V. Yang, C.G. Radu, M. Roy, S. Lee, J. McLaughlin, M.A. Teitell, M.L. Iruela-Arispe, O.N. Witte, Vascular abnormalities in mice deficient for the G protein-coupled receptor GPR4 that functions as a pH sensor, Mol. Cell. Biol. 27 (2007) 1334–1347.
[13] N. Thongon, P. Ketkeaw, C. Nuekchob, The roles of acid-sensing ion channel 1a and ovarian cancer G protein-coupled receptor 1 on passive Mg2+ transport across intestinal epithelium-like Caco-2 monolayers, J. Physiol. Sci. 64 (2014) 129–139.
[14] N. Mohebbi, C. Benabbas, S. Vidal, A. Daryadel, S. Bourgeois, A. Velic, M.G. Ludwig, K. Seuwen, C.A. Wagner, The proton-activated G protein coupled receptor OGR1 acutely regulates the activity of epithelial proton transport proteins, Cell. Physiol. Biochem. 29 (2012) 313–324.
[15] H. Saxena, D.A. Deshpande, B.C. Tiegs, H. Yan, R.J. Battafarano, W.M. Burrows, G. Damera, R.A. Panettieri, T.D. Dubose, S.S. An, R.B. Penn, The GPCR OGR1 (GPR68) mediates diverse signalling and contraction of airway smooth muscle in response to small reductions in extracellular pH, Br. J. Pharmacol. 166 (2012) 981–990.
[16] S. Matsuzaki, T. Ishizuka, H. Yamada, Y. Kamide, T. Hisada, I. Ichimonji, H. Aoki, M. Yatomi, M. Komachi, H. Tsurumaki, A. Ono, Y. Koga, K. Dobashi, C. Mogi, K. Sato, H. Tomura, M. Mori, F. Okajima, Extracellular acidification induces connective tissue growth factor production through proton-sensing receptor OGR1 in human airway smooth muscle cells, Biochem. Biophys. Res. Commun. 413 (2011) 499–503.
[17] I. Ichimonji, H. Tomura, C. Mogi, K. Sato, H. Aoki, T. Hisada, K. Dobashi, T. Ishizuka, M. Mori, F. Okajima, Extracellular acidification stimulates IL-6 production and Ca(2+) mobilization through proton-sensing OGR1 receptors in human airway smooth muscle cells, Am. J. Physiol. Lung Cell. Mol. Physiol. 299 (2010) L567–L577.
[18] J.P. Liu, M. Komachi, H. Tomura, C. Mogi, A. Damirin, M. Tobo, M. Takano, H. Nochi, K. Tamoto, K. Sato, F. Okajima, Ovarian cancer G protein-coupled receptor 1-dependent and -independent vascular actions to acidic pH in human aortic smooth muscle cells, Am. J. Physiol. Heart Circ. Physiol. 299 (2010) H731–H742.
[19] H. Tomura, J.Q. Wang, M. Komachi, A. Damirin, C. Mogi, M. Tobo, J. Kon, N. Misawa, K. Sato, F. Okajima, Prostaglandin I(2) production and cAMP accumulation in response to acidic extracellular pH through OGR1 in human aortic smooth muscle cells, J. Biol. Chem. 280 (2005) 34458–34464.

[20] A.V. Gore, K. Monzo, Y.R. Cha, W. Pan, B.M. Weinstein, Vascular development in the zebrafish, Cold Spring Harbor Perspect. Med. 2 (2012) a006684.
[21] M. Mione, A.H. Meijer, B.E. Snaar-Jagalska, H.P. Spaink, N.S. Trede, Disease modeling in zebrafish: cancer and immune responses–a report on a workshop held in Spoleto, Italy, July 20–22, 2009, Zebrafish 6 (2009) 445–451.
[22] H. Aoki, C. Mogi, T. Hisada, T. Nakakura, Y. Kamide, I. Ichimonji, H. Tomura, M. Tobo, K. Sato, H. Tsurumaki, K. Dobashi, T. Mori, A. Harada, M. Yamada, M. Mori, T. Ishizuka, F. Okajima, Proton-sensing ovarian cancer G protein-coupled receptor 1 on dendritic cells is required for airway responses in a murine asthma model, PLoS One 8 (2013) e79985.
[23] M. Kotake, K. Sato, C. Mogi, M. Tobo, H. Aoki, T. Ishizuka, N. Sunaga, H. Imai, K. Kaira, T. Hisada, M. Yamada, F. Okajima, Acidic pH increases cGMP accumulation through the OGR1/phospholipase C/Ca(2+)/neuronal NOS pathway in N1E-115 neuronal cells, Cell. Signal. 26 (2014) 2326–2332.
[24] O. Murch, M. Abdelrahman, M. Collino, M. Gallicchio, E. Benetti, E. Mazzon, R. Fantozzi, S. Cuzzocrea, C. Thiemermann, Sphingosylphosphorylcholine reduces the organ injury/dysfunction and inflammation caused by endotoxemia in the rat, Crit. Care Med. 36 (2008) 550–559.
[25] E. Afrasiabi, T. Blom, E. Ekokoski, R.K. Tuominen, K. Törnquist, Sphingosylphosphorylcholine enhances calcium entry in thyroid FRO cells by a mechanism dependent on protein kinase C, Cell. Signal. 18 (2006) 1671–1678.
[26] Y. Jin, B.B. Damaj, A.A. Maghazachi, Human resting CD16-, CD16+ and IL-2-, IL-12-, IL-15- or IFN-alpha-activated natural killer cells differentially respond to sphingosylphosphorylcholine, lysophosphatidylcholine and platelet-activating factor, Eur. J. Immunol. 35 (2005) 2699–2708.
[27] J. Qiao, F. Huang, R.P. Naikawadi, K.S. Kim, T. Said, H. Lum, Lysophosphatidylcholine impairs endothelial barrier function through the G protein-coupled receptor GPR4, Am. J. Physiol. Lung Cell. Mol. Physiol. 291 (2006) L91–L101.
[28] Y. Zou, C.H. Kim, J.H. Chung, J.Y. Kim, S.W. Chung, M.K. Kim, D.S. Im, J. Lee, B.P. Yu, H.Y. Chung, Upregulation of endothelial adhesion molecules by lysophosphatidylcholine. Involvement of G protein-coupled receptor GPR4, FEBS J. 274 (2007) 2573–2584.
[29] X. Sun, L.V. Yang, B.C. Tiegs, L.J. Arend, D.W. McGraw, R.B. Penn, S. Petrovic, Deletion of the pH sensor GPR4 decreases renal acid excretion, J. Am. Soc. Nephrol. 21 (2010) 1745–1755.
[30] J.Q. Wang, J. Kon, C. Mogi, M. Tobo, A. Damirin, K. Sato, M. Komachi, E. Malchinkhuu, N. Murata, T. Kimura, A. Kuwabara, K. Wakamatsu, H. Koizumi, T. Uede, G. Tsujimoto, H. Kurose, T. Sato, A. Harada, N. Misawa, H. Tomura, F. Okajima, TDAG8 is a proton-sensing and psychosine-sensitive G-protein-coupled receptor, J. Biol. Chem. 279 (2004) 45626–45633.
[31] K. Seuwen, M.G. Ludwig, R.M. Wolf, Receptors for protons or lipid messengers or both? J. Recept. Signal Transduction Res. 26 (2006) 599–610.
[32] H. Li, D. Wang, L.S. Singh, M. Berk, H. Tan, Z. Zhao, R. Steinmetz, K. Kirmani, G. Wei, Y. Xu, Abnormalities in osteoclastogenesis and decreased tumorigenesis in mice deficient for ovarian cancer G protein-coupled receptor 1, PLoS One 4 (2009) e5705.
[33] T. Nakakura, C. Mogi, M. Tobo, H. Tomura, K. Sato, M. Kobayashi, H. Ohnishi, S. Tanaka, M. Wayama, T. Sugiyama, T. Kitamura, A. Harada, F. Okajima, Deficiency of proton-sensing ovarian cancer G protein-coupled receptor 1 attenuates glucose-stimulated insulin secretion, Endocrinology 153 (2012) 4171–4180.
[34] L. Wyder, T. Suply, B. Ricoux, E. Billy, C. Schnell, B.U. Baumgarten, S.M. Maira, C. Koelbing, M. Ferretti, B. Kinzel, M. Müller, K. Seuwen, M.G. Ludwig, Reduced pathological angiogenesis and tumor growth in mice lacking GPR4, a proton sensing receptor, Angiogenesis 14 (2011) 533–544.
[35] L. Giudici, A. Velic, A. Daryadel, C. Bettoni, N. Mohebbi, T. Suply, K. Seuwen, M.G. Ludwig, C.A. Wagner, The proton-activated receptor GPR4 modulates glucose homeostasis by increasing insulin sensitivity, Cell. Physiol. Biochem. 32 (2013) 1403–1416.

LETTER

doi:10.1038/nature14215

YAP is essential for tissue tension to ensure vertebrate 3D body shape

Sean Porazinski[1]*, Huijia Wang[1]*, Yoichi Asaoka[2]*, Martin Behrndt[3]*, Tatsuo Miyamoto[4]*, Hitoshi Morita[3], Shoji Hata[2], Takashi Sasaki[5], S. F. Gabriel Krens[3], Yumi Osada[6], Satoshi Asaka[2], Akihiro Momoi[6], Sarah Linton[1], Joel B. Miesfeld[7], Brian A. Link[7], Takeshi Senga[8], Atahualpa Castillo-Morales[1], Araxi O. Urrutia[1], Nobuyoshi Shimizu[5], Hideaki Nagase[9], Shinya Matsuura[4], Stefan Bagby[1], Hisato Kondoh[6,10,11], Hiroshi Nishina[2], Carl-Philipp Heisenberg[3] & Makoto Furutani-Seiki[1,6]

Vertebrates have a unique 3D body shape in which correct tissue and organ shape and alignment are essential for function. For example, vision requires the lens to be centred in the eye cup which must in turn be correctly positioned in the head[1]. Tissue morphogenesis depends on force generation, force transmission through the tissue, and response of tissues and extracellular matrix to force[2,3]. Although a century ago D'Arcy Thompson postulated that terrestrial animal body shapes are conditioned by gravity[4], there has been no animal model directly demonstrating how the aforementioned mechano-morphogenetic processes are coordinated to generate a body shape that withstands gravity. Here we report a unique medaka fish (*Oryzias latipes*) mutant, *hirame* (*hir*), which is sensitive to deformation by gravity. *hir* embryos display a markedly flattened body caused by mutation of YAP, a nuclear executor of Hippo signalling that regulates organ size. We show that actomyosin-mediated tissue tension is reduced in *hir* embryos, leading to tissue flattening and tissue misalignment, both of which contribute to body flattening. By analysing YAP function in 3D spheroids of human cells, we identify the Rho GTPase activating protein ARHGAP18 as an effector of YAP in controlling tissue tension. Together, these findings reveal a previously unrecognised function of YAP in regulating tissue shape and alignment required for proper 3D body shape. Understanding this morphogenetic function of YAP could facilitate the use of embryonic stem cells to generate complex organs requiring correct alignment of multiple tissues.

Via exhaustive mutant screening in medaka and zebrafish[5,6], we identified medaka *hir* mutants displaying pronounced body flattening around stage (st.) 25–28 (50–64 h post fertilization, hpf; Fig. 1a). Although general development was not delayed, *hir* mutants exhibited delayed blastopore closure (Fig. 1b, c) and progressive body collapse from mid-neurulation (st. 20, 31 hpf) (Fig. 1d), surviving until just before hatching (6 days post-fertilization, dpf). During body collapse, tissues

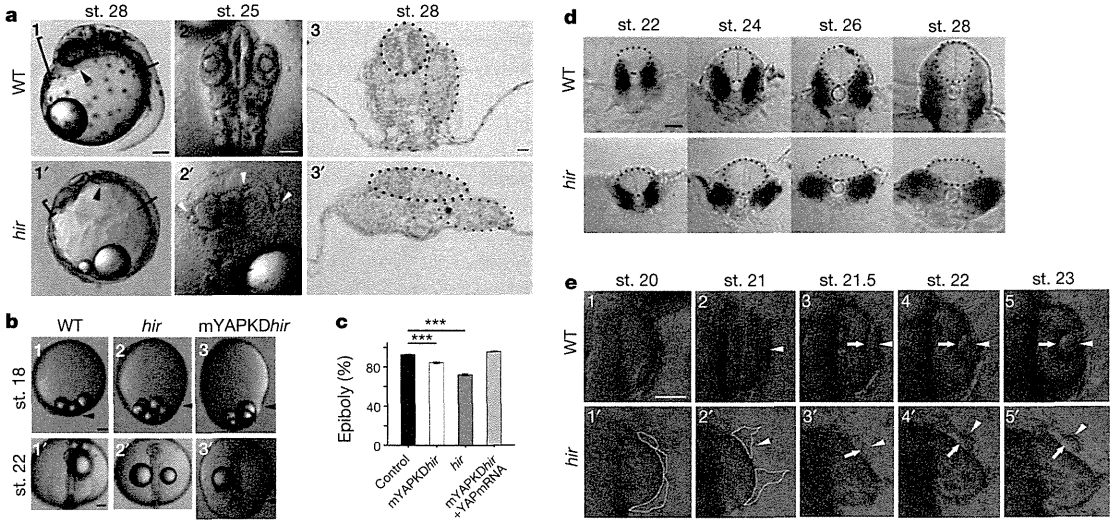

Figure 1 | Organ/tissue collapse and misalignment in *hir* mutants. **a1**, **a1′**, Lateral view of live WT and *hir* mutant embryos, anterior to the left. Arrowheads, heart. Brackets, embryo thickness. **a2**, **a2′**, Dorsal view, anterior upwards. Arrowheads, mislocated lenses. **a3**, **a3′**, Transverse section at the plane shown in **a1** and **a1′**. Neural tubes (black dots) and somites (red dots). **b1**–**b3**, Lateral and **b1′**–**b3′**, dorsal views of live embryos. Arrowheads, blastoderm margin. **c**, Quantification of epiboly (%). Error bars ± s.e.m. (***$P < 0.001$; one-way ANOVA with Dunnett's T3 post hoc. Fig. 1 Source Data). **d**, Transverse sections at 5th somite level, neural tube (encircled) and somites (blue) by *myoD in situ* hybridization. **e**, Time-lapse sequence of dorsal view of WT and *hir* mutant right eyes. Arrowheads, lens placode; arrows, invaginating retina. Fragmented and detaching lens placode demarcated by dotted lines in **e1′** and **e2′**. Scale bars, 40 μm.

[1]Department of Biology and Biochemistry, University of Bath, Bath BA2 7AY, UK. [2]Department of Developmental and Regenerative Biology, Medical Research Institute, Tokyo Medical and Dental University (TMDU), Tokyo 113-8510, Japan. [3]IST Austria, Am Campus 1, A-3400 Klosterneuburg, Austria. [4]Department of Genetics and Cell Biology, Research Institute for Radiation Biology and Medicine, Hiroshima University, Hiroshima 734-8553, Japan. [5]Department of Molecular Biology, School of Medicine, Keio University, Tokyo 160-8582, Japan. [6]Japan Science and Technology Agency (JST), ERATO-SORST Kondoh Differentiation Signaling Project, Kyoto 606-8305, Japan. [7]Department of Cell Biology, Neurobiology, and Anatomy, Medical College of Wisconsin, Milwaukee, Wisconsin 53226, USA. [8]Division of Cancer Biology, Nagoya University Graduate School of Medicine, Nagoya 466-8550, Japan. [9]Kennedy Institute of Rheumatology, Nuffield Department of Orthopaedics, Rheumatology and Musculoskeletal Sciences, University of Oxford, Oxford OX3 7FY, UK. [10]Graduate School of Frontier Bioscience, Osaka University, Osaka 565-0871, Japan. [11]Faculty of Life Sciences, Kyoto Sangyo University, Kyoto 603-8555, Japan.
*These authors contributed equally to this work.

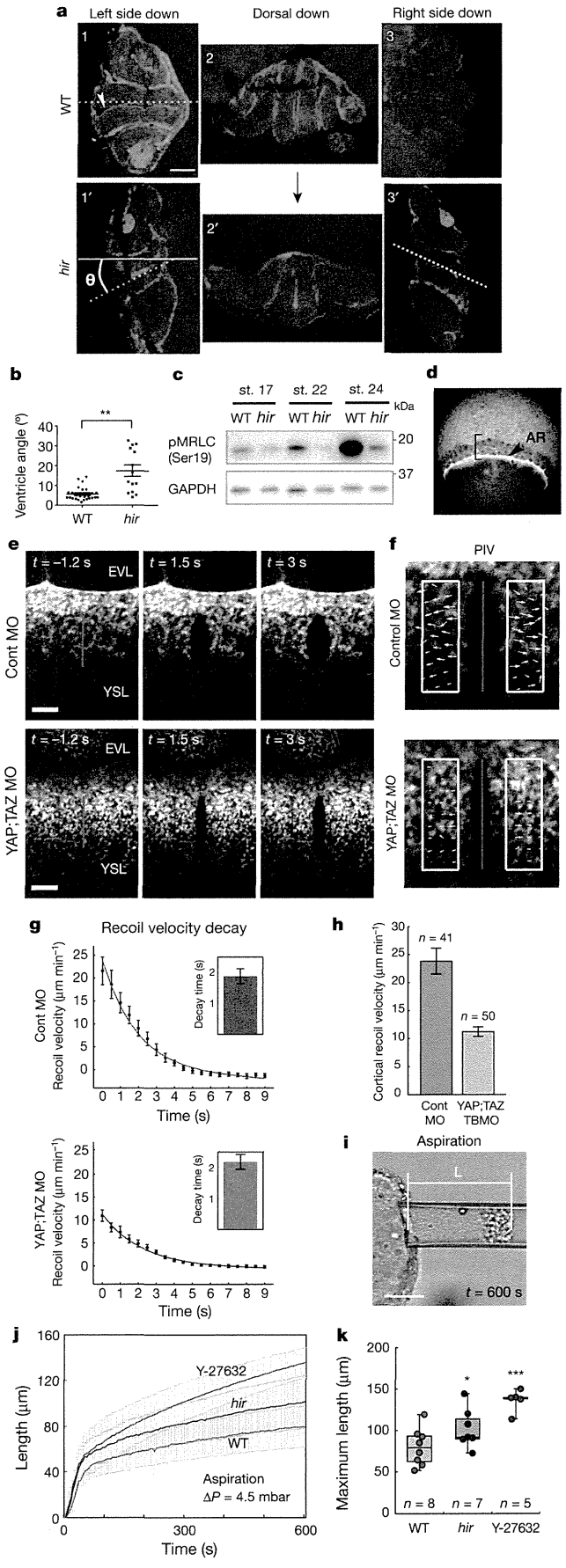

Figure 2 | Tissue tension is reduced in *hir* mutants. **a**, Embryos kept left side down (**a1**, **a1′**), dorsal facing down (**a2**, **a2′**) and right side down (**a3**, **a3′**) from st. 17–25, stained with phalloidin (green, F-actin) and TO-PRO-3 (blue, nucleus). Large black arrow, direction of gravity; θ, angle that the tangent along the brain ventricle (dotted lines in **a1**, **a1′**) makes with horizontal solid line. **b**, Range of collapse of mutant and WT embryos kept sideways. Error bars, ± s.e.m. $^{**}P < 0.01$, *t*-test (see Fig. 2 Source Data). **c**, Immunoblotting of phospho-myosin regulatory light chain (pMRLC, Ser19) and control (GAPDH) (Supplementary Fig. 1). **d**, Actomyosin-labelled *Tg(actb2:myl12.1-eGFP)* zebrafish embryos at 75% epiboly. Arrowhead, YSL actomyosin ring (AR) at the margin of the EVL. Bracket, for analysis of EVL shape anisotropy (Extended Data Fig. 3a). **e**, The actomyosin ring was cut along a 20 μm-long line (red) perpendicular to the EVL/YSL boundary in MO-injected embryos, when control MO injected embryos were at 70–80% epiboly. **f**, Particle image velocimetry (PIV) quantifies the velocity field (yellow arrows) of the recoiling actomyosin network. **g**, Averaged temporal recoil velocity curves, control MO ($n = 41$) and YAP;TAZ KD conditions ($n = 50$). Error bars, error of the mean at 95% confidence. Exponential fit function with a linear offset (black solid line) yields the characteristic decay time (inset) and **h**, the initial recoil velocity for the control MO (23.8 ± 2.3 μm min^{-1}) and YAP;TAZ KD conditions (11.2 ± 0.8 μm min^{-1}). Error bars, 95% confidence interval for the fit results. **i**, Snapshot at the end of aspiration (600 s) of st. 22 neural tube with constant pressure ($\Delta P = 4.5$ mbar). **j**, The curves of the tongue length over time to measure the aspiration of WT, *hir* mutant and ROCK inhibitor (Y27632)-treated neural tube explants. Error bars, ± s.d. Maximum tongue lengths measured at 600 s were compared by *t*-test in **k**. Box plots represent 5%, 25%, median, 75%, and 95%. $^{*}P < 0.05$, $^{***}P < 0.001$. Scale bars, 40 μm in **a**, **i**, 10 μm in **e**.

and organs including neural tube and somites gradually became flattened and improperly aligned (Fig. 1d). Lenses were misaligned outside the eyes (Fig. 1a2, a2′). Mutant lens placodes expressing *sox3* formed normally adjacent to the retina up to st. 20, but then became fragmented and detached from the retina (Fig. 1e1′, e2′, Extended Data Fig. 1a, b and Supplementary Videos 1, 2). These fragments gradually rounded up with some re-attaching to the retina to form ectopic lenses that were not incorporated (Fig. 1e). Thus, tissue flattening and misalignment defects are associated with the flattened mutant phenotype.

Positional cloning identified a nonsense mutation of Leu164 (TTG to TAG) in the WW1 domain of YAP in *hir* (Extended Data Fig. 1c, d). YAP is the nuclear executor of the Hippo pathway and regulates organ growth via stimulation of cell proliferation[7–9]. In wild-type (WT) embryos, YAP transcripts are ubiquitous throughout development[10]. Medaka maternal *YAP* messenger RNA (mRNA) was present at st. 10 in *hir* before onset of zygotic gene expression, but undetectable after st. 18 (Extended Data Fig. 1e). Morpholino oligonucleotide (MO) YAP knockdown (KD) in WT embryos recapitulated the *hir* phenotype (Extended Data Fig. 2a–c, Supplementary Tables 1, 2), and ubiquitous recombinant *YAP* mRNA expression rescued the *hir* phenotype (Extended Data Fig. 1f). In addition, perturbation of maternal *YAP* mRNA translation in *hir* mutant embryos by YAP translation-blocking (TB) MO (mYAP KD *hir* embryos) elicited a more severe blastopore closure and body flattening phenotype than in *hir* zygotic YAP mutants (Fig. 1b3, b3′, c, Supplementary Table 2). Blastopore closure defects, but not flattening, have been reported in YAP KD zebrafish and *Xenopus*[11]. Since TAZ is a functional paralogue of YAP[12], we evaluated its contribution to the YAP KD phenotype in zebrafish. YAP;TAZ double KD zebrafish embryos exhibited more pronounced blastopore closure defects than YAP KD alone (Extended Data Fig. 2d–h). YAP-4SA, which lacks four serines and predominantly localizes to the nucleus[13], rescued the *hir* phenotype more efficiently than WT YAP (Extended Data Fig. 1f), suggesting that the *hir* phenotype depends on nuclear YAP. The main nuclear function of YAP is to promote proliferation and inhibit cell death[14]. *hir* embryos had increased cell death from st. 22 to 26 after body flattening had initiated (increased cell death per se does not lead to body flattening[5,6]). Cell proliferation remained close to normal in *hir* embryos but was strongly suppressed in TAZ KD (and YAP/TAZ double KD) medaka embryos (Extended Data Fig. 2i, j). Thus, in medaka, cell

proliferation is mainly regulated by TAZ, while YAP is predominantly required for 3D body shape.

Three dpf *hir* mutants showed different orientations of body flattening. We therefore examined whether collapse correlated with the direction of gravity. Mutant embryos maintained either right-side or left-side down relative to the earth collapsed towards the earth as indicated by the ventricle tangent (Fig. 2a). Average collapse angle, θ, in mutant embryos was $17.3 \pm 10.7^{\circ}$ ($n = 14$; Fig. 2b) compared to $5.6 \pm 3.3^{\circ}$ ($n = 26$, $P < 0.01$) in WT. Mutant embryos maintained dorsal side down exhibited apparently uniform dorso-ventral compression (Fig. 2a2, a2′). Thus, flattening in *hir* embryos reflects an inability to withstand external forces (that is, gravity), suggesting reduced tissue tension.

Tissue tension is generated primarily by actomyosin contraction[15]. During WT organogenesis, global levels of phosphorylated myosin regulatory light chain (pMRLC), indicative of actomyosin activity, increased (Fig. 2c), while in *hir* mutants they began decreasing as the blastopore closes (st. 17, 25 hpf), and continued decreasing coincident with tissue collapse and body flattening. To assess tissue tension during blastopore closure, we analysed a surface epithelial cell layer, the enveloping layer (EVL)[16] (Extended Data Fig. 3a1). Comparison of EVL shape anisotropy between WT and *hir* embryos suggested that tissue tension in *hir* is reduced within the EVL (Extended Data Fig. 3a, b). We also quantified actomyosin network tension within the yolk syncytial layer (YSL) of zebrafish embryos with compromised YAP function expressing enhanced green fluorescent protein (EGFP)–myosin light chain protein, Tg(*actb2:myl12.1-eGFP*)[17]. The YSL actomyosin network close to the EVL margin (Fig. 2d) was cut along a 20-μm-long line perpendicular to the margin to reveal circumferential tension (Fig. 2e). Recoil velocities were significantly reduced in YAP;TAZ KD ($n = 50$) compared to control KD embryos ($n = 41$; $11.2 \pm 0.8\ \mu m\ min^{-1}$ vs $23.8 \pm 2.3\ \mu m\ min^{-1}$) (Fig. 2f–h), suggesting reduced actomyosin network tension. Consistent with this, epiboly movements in YAP;TAZ double KD zebrafish embryos were significantly reduced (KD embryos: $53.63 \pm 3.93\%$; control embryos: $70.0 \pm 2.18\%$ deep cell epiboly). To test whether reduced actomyosin network tension is also responsible for neural tube tissue flattening in *hir*, we performed micropipette aspiration experiments[18]. *hir* neural explants were significantly less resistant than WT to external forces applied by aspiration, indicating reduced neural tube tissue tension. The higher deformability of *hir* neural tube tissue was paralleled when myosin activity was reduced by ROCK inhibition (Fig. 2i–k). Together, these analyses indicate that YAP is required for actomyosin-mediated tissue tension in medaka and zebrafish.

Single-cell tracking analysis of the growing neural tube in *hir* showed that tissue flattening was associated with failure to stack cells, and increase in cells slipping to one side after perpendicular cell division (Fig. 3a, Extended Data Figs 4, 5). Live imaging showed loss of filopodia that tether lens to retina during lens invagination[1] (Extended Data Figs 1b, 6a, b). The formation of lens–retina filopodia requires fibronectin (FN)-integrin signalling and contractile actomyosin[1]. While st. 22 WT embryos had elongated thin FN fibrils between invaginating lens and retina, *hir* retina showed punctate FN patches (Fig. 3b1″, b2″), suggesting defective FN fibril formation. In addition, large ectopic FN deposits were found on the retina in *hir* (Fig. 3b2′). Similar loss of normal FN fibrils and formation of large FN deposits were observed throughout *hir* embryos (Fig. 3b4′, b5′). Furthermore, integrin β1 accumulation between lens and retina was lost in *hir* (Extended Data Fig. 6c). In contrast, cell–cell adhesion and apical markers, including pan-cadherin, atypical PKC (aPKC) and ZO-1, were unaltered in *hir* (data not shown). Mosaic expression of YAP in *hir* and transplantation experiments both showed that the *hir* mutation acts in a non-cell-autonomous manner (Extended Data Fig. 7, Supplementary Table 4). For instance, in invaginated *hir* lens rescued by mosaic expression of YAP, non-YAP expressing *hir* cells recovered filopodia (Extended Data Figs 7b, 6b). These data suggest that YAP functions in tissue alignment by regulating FN assembly.

To identify downstream YAP effectors regulating tissue tension, we used a human 3D spheroid *in vitro* culture system employing the human retina pigmented epithelial cell line hTERT-RPE1 (RPE1), which displayed a relatively mild proliferation defect upon YAP KD. YAP KD spheroids collapsed upon exposure to external forces by slow centrifugation, unlike normal spheroids (Fig. 4a, b). pMRLC levels were reduced in YAP KD spheroids (Fig. 4c), as in *hir*, suggesting that YAP maintains tissue tension also in human 3D tissues. YAP KD spheroids also lacked the typical beehive-like pattern of FN fibrils and, instead, contained large FN deposits, reminiscent of the *hir* retina phenotype

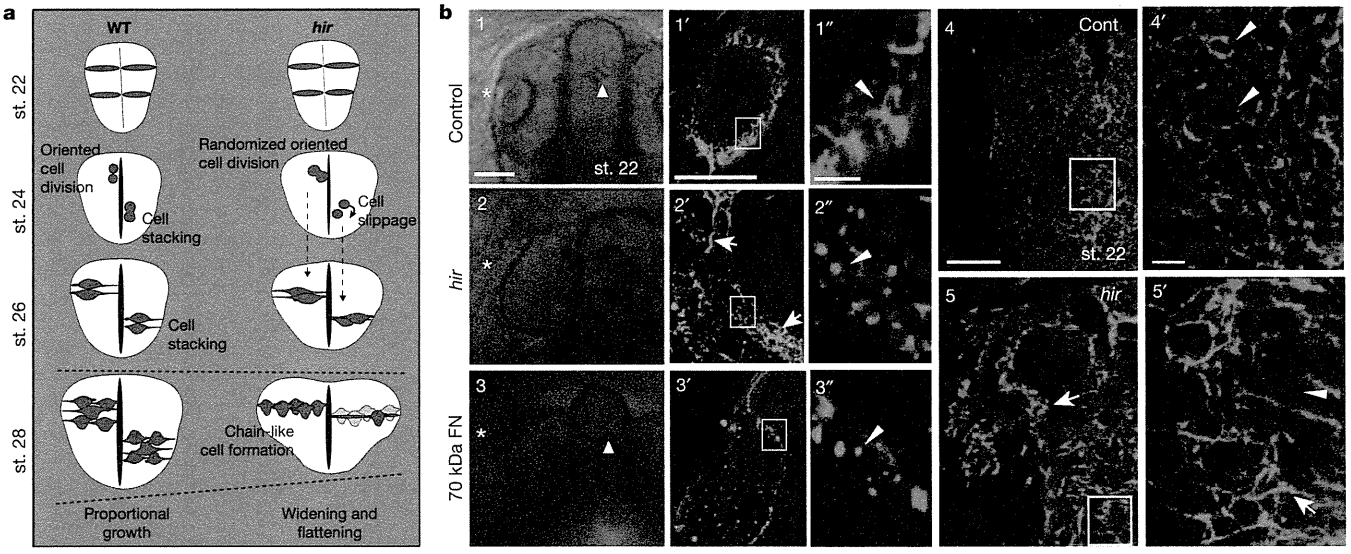

Figure 3 | Cell and tissue dynamics in *hir* mutants. **a**, Schematic: *hir* neural tube collapse is associated with long chain-like arrangements of neuroepithelial cells generated by increased cell slippage and randomized oriented cell division (Extended Data Figs 4, 5). **b**, Whole-mount FN immunohistochemistry (IHC) of st. 22 embryos, dorsal view, anterior to the top. **b1–b1″**, WT embryos injected with out-of-frame 70 kDa N-terminal medaka FN1a+1b mRNA (250 pg) ($n = 20$); **b2–b2″**, uninjected *hir* mutants ($n = 11$); **b3–b3″**, WT embryos injected with N-terminal 70kDa FN1a+1b mRNA (250 pg) ($n = 39$). **b1–b3**, Left anterior head of live embryos (asterisks, lens; triangle, forebrain ventricle); **b1′–b3′**, left eye of FN IHC (green), boxed area magnified in **b1″–b3″**; **b4**, **b5**, surface view of FN stained neural tube, WT ($n = 15$) and *hir* ($n = 14$) corresponding to the region in 1 and 2, respectively, boxed area magnified in **b4′** and **b5′**. Arrowheads, FN fibrils/puncta; arrows, FN large deposits. Scale bars, 40 μm in **b1**, **b1′**, **b4**; 5 μm in **b1″**, **b4′**.

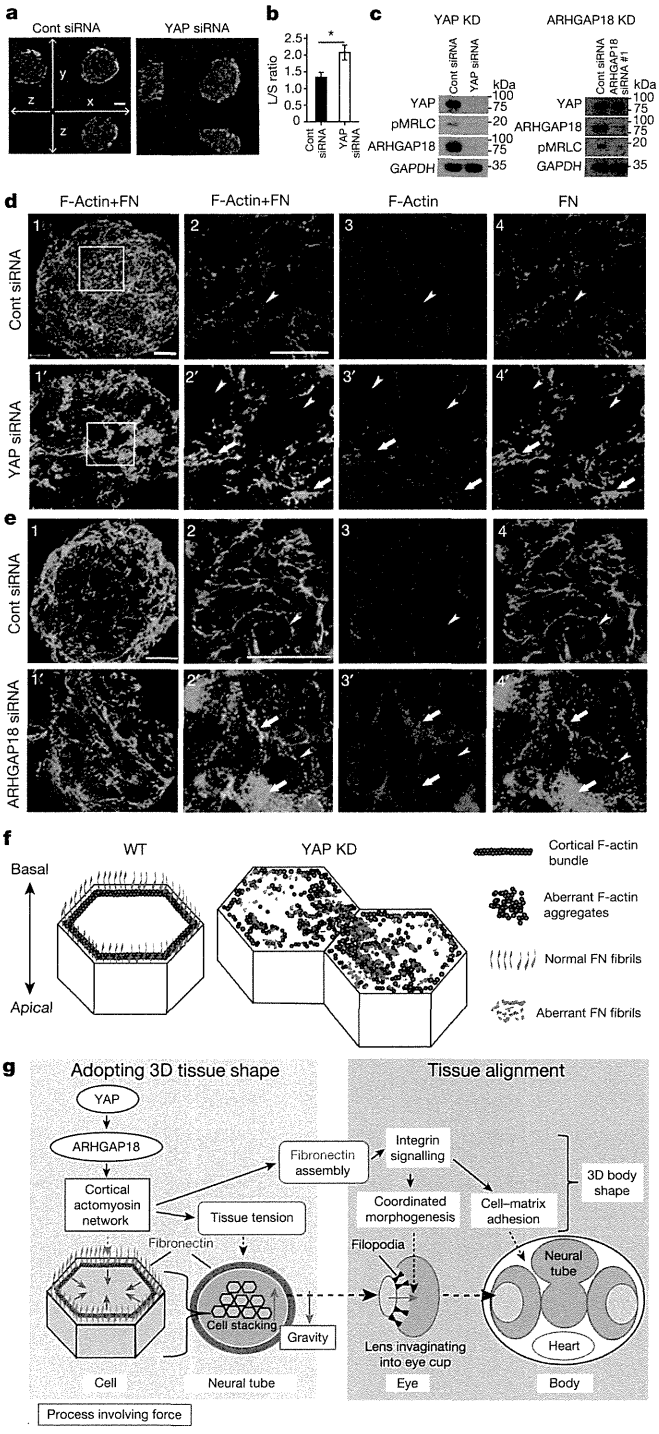

Figure 4 | YAP regulation of tissue tension and FN assembly is mediated by ARHGAP18. **a**, **b**, Confocal 3D sectioning of longest and shortest axes of YAP and control (Cont) KD RPE1 spheroids ($n = 5, 7$) after centrifugation. **b**, Ratio of longest (L)/shortest (S) axes. Error bars, ± s.e.m. $^*P < 0.05$, *t*-test (Fig. 4 Source Data). **c**, Immunoblotting of YAP and ARHGAP18 KD spheroids for the indicated proteins (Supplementary Fig. 1). **d**, **e**, Whole-mount imaging of basal surfaces of spheroids transfected with control siRNA ($n = 17$), YAP siRNA ($n = 13$), and ARHGAP18 siRNA ($n = 15$), stained for F-actin (red) and FN (green). **d2**–**d4**, Magnified view of boxed areas in **d1**. Arrowheads, cortical regions; arrows, ectopic F-actin aggregates and aberrant FN fibrils. **f**, Schematic; fine extracellular FN fibrils form in close proximity to cortical F-actin in normal cells, while in YAP and ARHGAP18 KD cells, FN fibrils are reduced and aberrant FN deposits coincide with ectopic F-actin aggregates. **g**, Schematic summarizing how YAP/ARHGAP18-dependent actomyosin network contraction controls tissue shape and alignment. Scale bars, 40 μm in **a**; 30 μm in **d1**, **e1**; 15 μm in **d2**, **e2**.

(Fig. 4d). Cortical actomyosin contraction is required for polymerizing FN monomers to form fibrils[19,20]; consistently, FN fibril formation on the basal surface of control spheroids coincided with cortical F-actin bundles (Fig. 4d). In contrast, loss of normal FN fibrils in YAP KD spheroids was associated with marked reduction of cortical F-actin bundles (Fig. 4d, f). Instead, we observed F-actin aggregates, some of which were associated with large FN deposits, suggesting that they have increased local tension (Fig. 4d). A similar distribution of F-actin and FN was observed in *hir* (Extended Data Fig. 8a). Gene expression profiling of YAP KD spheroids identified only forty genes with reduced expression (see Methods), including *ARHGAP18*, encoding a Rho GTPase activating protein that suppresses F-actin polymerization by inhibiting Rho[21]. *ARHGAP18* transcripts and protein levels were reduced in YAP KD spheroids (Fig. 4c), and ARHGAP18 KD spheroids exhibited a similar phenotype to YAP KD spheroids, including reduced pMRLC levels (Fig. 4c) and aberrant F-actin and FN assembly (Fig. 4e). This suggests that both disruption of cortical F-actin bundles and formation of ectopic F-actin aggregates (Fig. 4f) arise from F-actin over-polymerization in YAP KD spheroids (Extended Data Fig. 8b) and ARHGAP18 KD cells. Together, these results suggest that ARHGAP18 acts downstream of YAP and is required for cortical actomyosin network formation and tissue tension.

To analyse the contribution of actomyosin tension-mediated FN assembly defects to the *hir* eye phenotype, we blocked FN assembly to a similar extent to that in *hir* by overexpressing 70-kDa amino-terminal FN1a and FN1b fragments in WT embryos[22] (Fig. 3b3′, b3′′); this caused near dislocation of the lens and fewer filopodia between lens and retina (Fig. 3b3). *hir* mutants had fewer filopodia than FN assembly blocked embryos (Extended Data Fig. 6a, b), suggesting that contractile actomyosin defects in *hir* exacerbate the incomplete lens dislocation caused by FN assembly defects. In contrast, FN assembly blocked embryos did not exhibit flattened tissues (Fig. 3b1–b3). Furthermore, the medaka FN1 mutant *fukuwarai* (*fku*) also exhibited lens dislocation but not tissue flattening (Extended Data Fig. 8c), suggesting that FN is specifically required for tissue alignment, but not generally for YAP-dependent tissue shape. *ARHGAP18* mRNA levels were significantly reduced in *hir*, and mRNA injection of plasma membrane-targeted myristoylated ARHGAP18 (*myrARHGAP18*) into *hir* substantially rescued FN assembly defects, lens invagination and body flattening (Extended Data Fig. 9a, b). In contrast, inactivation of ARHGAP18 alone was insufficient to produce a recognizable phenotype (data not shown), suggesting that multiple ARHGAP18-related genes function downstream of YAP in medaka embryos. Consistently, short interfering RNA (siRNA) knockdown screening in human cells identified five ARHGAP genes with similar functions to ARHGAP18, homologues of which are conserved in medaka and zebrafish (Extended Data Fig. 9c, d and Supplementary Discussion). These results suggest that ARHGAP18-related genes function as effectors of YAP essential for both tissue shape and FN-dependent tissue alignment. The *hir* phenotype is not simply due to reduced myosin contraction, because injecting mRNA of an activated form of MRLC-DD[23] did not rescue the *hir* phenotype (Extended Data Figs 3a6, b, 8d). Similarly, injection of dominant negative MRLC-AA[23] in WT embryos failed to fully phenocopy the *hir* tissue or body flattening phenotype (Extended Data Fig. 3a5, b). Collectively, these results suggest that YAP function in 3D tissue shape and FN assembly is conserved in human cells and is at least partly mediated by ARHGAP18-related genes.

We propose that YAP is essential for tissue tension, acting through ARHGAP18 and related genes to regulate cortical actomyosin network formation (Fig. 4g). YAP-dependent actomyosin network tension is required for both proper tissue shape and alignment to ensure organ/body shape. Several upstream regulators of YAP-mediated cell proliferation

have been identified, including cellular environment stiffness, suggesting that YAP can function as a mechanosensor[24]. Our data show that YAP also functions as a mechanoregulator of tissue tension. Reduced cortical actomyosin tension is the most probable cause of attenuated tissue tension in *hir* mutants. F-actin over-polymerization perturbs F-actin turnover required for actomyosin contraction in the cytokinetic ring[25]. Our finding that ARHGAP18, a suppressor of F-actin polymerization, functions downstream of YAP further supports a critical role of F-actin polymerization in contractile actomyosin network formation. YAP is required for basal-level actomyosin activity, consistent with ubiquitous expression of actin modulator ARHGAP18[21], additional to which spatiotemporal modulation of actomyosin activity defines tissue shape. Since ARHGAP18 suppresses actin polymerization, which in turn reduces nuclear localization of YAP[26], ARHGAP18 might suppress YAP activity via a negative feedback mechanism. This points to a possible mechanical feedback loop where tissue tension controls YAP, and YAP in turn is required for tissue tension.

Actomyosin contraction promotes FN assembly[27]. The tissue misalignment phenotype in *hir* is most likely owing to failure of YAP-dependent actomyosin contractility in controlling FN assembly. Since FN initiates extracellular matrix organization[27], actomyosin contraction-mediated FN assembly could be a critical *in vivo* mechanism that integrates mechanical signals (for example, tension generated by actomyosin) with biochemical signals (for example, integrin signalling). Notably, the phenotype of YAP KO mouse embryos resembles that of FN KO mouse embryos[28], suggesting that YAP and FN have similar functions in mouse development. Interestingly, while YAP in medaka is predominantly required for tissue tension, its paralogue TAZ seems to be required for cell proliferation (Supplementary Discussion). Given the high degree of conservation of YAP and other Hippo pathway components across metazoa[29], it will be worth investigating whether the extent of tissue three-dimensionality and alignment correlate with the emergence of YAP-mediated resistance to gravity at the evolutionary transition from uni- to multicellular organisms. Finally, generation of a simple organ, such as an eye cup, from induced pluripotent/embryonic stem cells depends on tissue self-organization involving force-mediated processes for which the mechanism remains elusive[30]. Our finding that YAP-dependent force-mediated morphogenesis is required not only for 3D tissue morphogenesis but also tissue alignment suggests that YAP-dependent force-mediated morphogenesis could be involved in self-organization of multiple tissues. Hence, our findings could have implications for the generation of complex organs comprising multiple tissues from induced pluripotent/embryonic stem cells.

Online Content Methods, along with any additional Extended Data display items and Source Data, are available in the online version of the paper; references unique to these sections appear only in the online paper.

Received 26 August; accepted 29 December 2014.
Published online 16 March 2015.

1. Chauhan, B. K. *et al.* Cdc42- and IRSp53-dependent contractile filopodia tether presumptive lens and retina to coordinate epithelial invagination. *Development* **136,** 3657–3667 (2009).
2. Nelson, C. M. & Bissell, M. J. Of extracellular matrix, scaffolds, and signaling: tissue architecture regulates development, homeostasis, and cancer. *Annu. Rev. Cell Dev. Biol.* **22,** 287–309 (2006).
3. Mammoto, T. & Ingber, D. E. Mechanical control of tissue and organ development. *Development* **137,** 1407–1420 (2010).
4. Thompson, D. W. *On Growth and Form* (Cambridge Univ. Press, 1917).
5. Furutani-Seiki, M. *et al.* Neural degeneration mutants in the zebrafish, *Danio rerio*. *Development* **123,** 229–239 (1996).
6. Furutani-Seiki, M. *et al.* A systematic genome-wide screen for mutations affecting organogenesis in medaka, *Oryzias latipes*. *Mech. Dev.* **121,** 647–658 (2004).
7. Sudol, M. *et al.* Characterization of the mammalian YAP (Yes-associated protein) gene and its role in defining a novel protein module, the WW domain. *J. Biol. Chem.* **270,** 14733–14741 (1995).
8. Pan, D. The Hippo signaling pathway in development and cancer. *Dev. Cell* **19,** 491–505 (2010).
9. Zhao, B., Tumaneng, K. & Guan, K.-L. L. The Hippo pathway in organ size control, tissue regeneration and stem cell self-renewal. *Nature Cell Biol.* **13,** 877–883 (2011).
10. Miesfeld, J. B. & Link, B. A. Establishment of transgenic lines to monitor and manipulate Yap/Taz-Tead activity in zebrafish reveals both evolutionarily conserved and divergent functions of the Hippo pathway. *Mech. Dev.* **133,** 177–188 (2014).
11. Gee, S. T., Milgram, S. L., Kramer, K. L., Conlon, F. L. & Moody, S. A. Yes-associated protein 65 (YAP) expands neural progenitors and regulates Pax3 expression in the neural plate border zone. *PLoS ONE* **6,** e20309 (2011).
12. Lei, Q. Y. *et al.* TAZ promotes cell proliferation and epithelial-mesenchymal transition and is inhibited by the Hippo pathway. *Mol. Cell. Biol.* **28,** 2426–2436 (2008).
13. Zhao, B., Li, L., Tumaneng, K., Wang, C. Y. & Guan, K.-L. L. A coordinated phosphorylation by Lats and CK1 regulates YAP stability through $SCF^{\beta\text{-}TRCP}$. *Genes Dev.* **24,** 72–85 (2010).
14. Heisenberg, C.-P. P. & Bellaïche, Y. Forces in tissue morphogenesis and patterning. *Cell* **153,** 948–962 (2013).
15. Vicente-Manzanares, M., Ma, X., Adelstein, R. S. & Horwitz, A. R. Cytoskeletal motors: non-muscle myosin II takes centre stage in cell adhesion and migration. *Nature Rev. Mol. Cell Biol.* **10,** 778–790 (2009).
16. Köppen, M., Fernández, B. G., Carvalho, L., Jacinto, A. & Heisenberg, C.-P. P. Coordinated cell-shape changes control epithelial movement in zebrafish and *Drosophila*. *Development* **133,** 2671–2681 (2006).
17. Behrndt, M. *et al.* Forces driving epithelial spreading in zebrafish gastrulation. *Science* **338,** 257–260 (2012).
18. Guevorkian, K., Colbert, M.-J., Durth, M., Dufour, S. & Brochard-Wyart, F. Aspiration of biological viscoelastic drops. *Phys. Rev. Lett.* **104,** 218101 (2010).
19. Singh, P., Carraher, C. & Schwarzbauer, J. E. Assembly of fibronectin extracellular matrix. *Annu. Rev. Cell Dev. Biol.* **26,** 397–419 (2010).
20. Rolo, A., Skoglund, P. & Keller, R. E. Morphogenetic movements driving neural tube closure in *Xenopus* require myosin IIB. *Dev. Biol.* **327,** 327–338 (2009).
21. Maeda, M. *et al.* ARHGAP18, a GTPase-activating protein for RhoA, controls cell shape, spreading, and motility. *Mol. Biol. Cell* **22,** 3840–3852 (2011).
22. McDonald, J. A. *et al.* Fibronectin's cell-adhesive domain and an amino-terminal matrix assembly domain participate in its assembly into fibroblast pericellular matrix. *J. Biol. Chem.* **262,** 2957–2967 (1987).
23. Iwasaki, T., Murata-Hori, M., Ishitobi, S. & Hosoya, H. Diphosphorylated MRLC is required for organization of stress fibers in interphase cells and the contractile ring in dividing cells. *Cell Struct. Funct.* **26,** 677–683 (2001).
24. Dupont, S. *et al.* Role of YAP/TAZ in mechanotransduction. *Nature* **474,** 179–183 (2011).
25. Pinto, I. M., Rubinstein, B., Kucharavy, A., Unruh, J. R. & Li, R. Actin depolymerization drives actomyosin ring contraction during budding yeast cytokinesis. *Dev. Cell* **22,** 1247–1260 (2012).
26. Sansores-Garcia, L. *et al.* Modulating F-actin organization induces organ growth by affecting the Hippo pathway. *EMBO J.* **30,** 2325–2335 (2011).
27. Daley, W. P., Peters, S. B. & Larsen, M. Extracellular matrix dynamics in development and regenerative medicine. *J. Cell Sci.* **121,** 255–264 (2008).
28. Morin-Kensicki, E. M. *et al.* Defects in yolk sac vasculogenesis, chorioallantoic fusion, and embryonic axis elongation in mice with targeted disruption of Yap65. *Mol. Cell. Biol.* **26,** 77–87 (2006).
29. Hilman, D. & Gat, U. The evolutionary history of YAP and the Hippo/YAP pathway. *Mol. Biol. Evol.* **28,** 2403–2417 (2011).
30. Sasai, Y. Cytosystems dynamics in self-organization of tissue architecture. *Nature* **493,** 318–326 (2013).

Supplementary Information is available in the online version of the paper.

Acknowledgements We thank M. Raff, T. Perry, A. Ward, M. Wills, J. Caunt, J. Clarke, L. Hurst and C. Tickle for critical reading and comments. We thank M. Tada, M. Furuse, N. Wada, Y. Nakai, J. Robinson and R. Kelsh for contributions to the paper and University of Bath for fish and bioimaging facilities. This work was funded by the ERATO/SORST projects of JST, Japan (H.K.), National Institutes of Health R01EY014167 (B.A.L.) and Medical Research Council, UK (M.F.-S.).

Author Contributions S.P., H.W., Y.A., M.B., T.M., H.M., S.H., T.S., S.F.G.K., Y.O., S.A., A.M., S.L., J.B.M., B.A.L., T.S., A.C.M., A.O.U., S.B. and M.F.-S. performed experiments. S.P., H.W., Y.A., M.B., T.M. and M.F.-S. conceived the study. S.B., N.S., H.N., S.M., H.K., C.-P.H., H.N. and M.F.- S. supervised the study. C.-P.H. and M.F.- S. wrote the paper. All authors interpreted data.

Author Information Reprints and permissions information is available at www.nature.com/reprints. The authors declare no competing financial interests. Readers are welcome to comment on the online version of the paper. Correspondence and requests for materials should be addressed to C.-P.H. (heisenberg@ist.ac.at), H.N. (nishina.dbio@mri.tmd.ac.jp) or M.F.-S. (furutaniseiki@gmail.com).

METHODS

Fish maintenance and fish strains. Medaka (*Oryzias latipes*) and zebrafish (*Danio rerio*) strains were maintained and raised according to previously published procedures[31]. Medaka and zebrafish embryos were raised in E3 solution at 28 °C. Fish care and procedures were approved by the University of Bath Ethical Review Committee, and are in compliance with the Animals Scientific Procedures Act 1986 of the UK. Medaka WT strains K-Cab, K-Kaga, and the mutant strain $hir^{54\text{-}20C}$, $fku^{8\text{-}33A}$, were used[6]. Zebrafish WT strain AB and *Tg(actb2:myl12.1-eGFP)*[32], that allow visualization of myosin, were used.

Embryological experiments. For fixation and live imaging, embryos were anaesthetized with 0.01% tricaine. For live imaging, embryos were embedded in 0.8% low melting temperature agarose (Type IV-A, Sigma, USA) in 35 mm glass-base dishes (Iwaki, Japan) at 28 °C. Standard embryological procedures including, dechorionation, fixation, *in situ* hybridization, immunohistochemistry, microinjection and cell transplantation were carried out according to previously published procedures[31]. Cells were transplanted to the region fated to become the eye and Cuvier's duct according to our fate map[33].

Positional cloning of *hir*. The *hir* mutation induced in the K-Cab strain was crossed with the polymorphic K-Kaga strain to carry out genetic mapping according to a previously published procedure[34]. To map the *hir* mutation on the chromosome, bulked segregant analysis was performed using M-markers[35] on DNA isolated from 48 homozygous mutant embryos and 48 WT siblings from F_2 embryos of mutant × K-Kaga mapping crosses.

Chromosome walking on chromosome 13 was performed using restriction fragment length polymorphism markers between K-Cab and K-Kaga strains to map to the two BAC clones. For fine mapping, 1,908 meioses were analysed to identify 9 recombinants mapping *hir* mutation close to *YAP*. *YAP* complementary DNA was amplified from *hir* mutants by RT–PCR and sequenced directly to identify the mutation.

RT–PCR cDNA cloning and construction. Total RNAs were isolated using TRIzol (Life Technologies) and were converted to cDNA using the RNA-PCR kit ver.3 (Takara Bio, Japan) followed by PCR using KOD plus polymerase (Toyobo, Japan). For mRNA production, PCR amplified full-length cDNAs (medaka *YAP, 70KDaFN1a,b, ARHGAP18*) were cloned into pCS2+ and for *in situ* hybridization medaka *sox3* cDNA was cloned into pBluescript II SK(−). *pCS2+myr-ARHGAP18* was constructed by adding the myristoylation sequence using oligonucleotides to produce myristoylated *ARHGAP18* mRNA. mRNAs were synthesized using SP6 mMESSAGE mMACHINE Kit (Ambion, USA). Primer sequences are shown in Supplementary Table 5.

Gravity experiment. Dechorionated embryos were embedded in 0.8% low melting temperature agarose in three orientations against gravity at st. 17, fixed at st. 25 and subjected to cryosectioning to determine the direction of tissue/organ collapse. Collapse of embryos towards gravity was assessed using images of sections stained with TO-PRO-3 and phalloidin.

Microinjection. mRNA, DNA and Morpholino were injected at 1-cell or 8-cell stages to deliver them to all cells or in a mosaic manner. The volume of one-shot of injection was 0.5 nl.

Phenotypic rescue experiments. Embryos from $hir^{+/-}$ heterozygote crosses were injected with mRNA of YAP variants. For transplantation phenotypic rescue experiments, embryos were genotyped by PCR using primers (Supplementary Table 5).

Morpholino KD analysis in medaka and zebrafish. Morpholino oligonucleotide (MO) from Gene Tools (USA) were used (Supplementary Table 6). Specificity of KD by MO was confirmed in a slightly different manner in medaka and zebrafish. Since rescue of the phenotype by mRNA injection did not work effectively in zebrafish, three different types of MOs, translation blocking (TB), splicing blocking (SB) and 5′ UTR MOs, were used and all were confirmed to induce a similar phenotype. In medaka, TB and SB MOs were used, and the phenotype was rescued by co-injecting corresponding mRNAs. To determine efficiency of KD, semiquantitative RT–PCR was carried out using primers that distinguish defective splicing from normal forms of mRNA (Supplementary Table 5).

Immunohistochemistry. Embryos were fixed in either 4% paraformaldehyde (PFA), Dent fixative or 1% TCA for 1–3 days and subjected to cryosectioning as described previously[31]. Antibodies used were: anti-FN antibody (Ab), Sigma F3648 at 1:100; β-integrin monoclonal Ab, 8c8 (Developmental Studies Hybridoma Bank, USA) at 1:10; anti-aPKC C-20 (SC216, Santa Cruz Biotech, USA) at 1:100; anti-PCNA (PC10, Santa Cruz Biotech, USA) at 1:500; anti-laminin (Ab-1, NeoMarkers, USA) at 1:100 and anti-ZO-1[36] (gift from M. Itoh) at 1:1. Sections were counterstained with Alexa Fluor 488 or 546 Phalloidin (A12379, A22283, Invitrogen USA) at 1:250 and TO-PRO-3 (T3605, Invitrogen, USA) at 1:1,000.

Time-lapse microscopy and image analysis. Time-lapse analysis of lens dislocation was carried out using a Leica MZ16FA dissecting microscope. Confocal microscopy used a Leica TCS SP5 and images were analysed by Imaris 7.3 (Bitplane, ANDOR Technology, UK) and Amira 5.1 (Visage Imaging, USA). Cell division orientation (θ) of telophase cells in time-lapse sequences was determined by drawing an axis from the ventricular zone-attached non-moving daughter cell (asterisk Extended Data Fig. 5c) towards the non-attached moving daughter cell[37]. The acute angle of this axis was then measured against the axis of the ventricular zone. Imaging was carried out dorsal side down using an inverted microscope. Rose diagrams were generated using Oriana v4 (Kovach Computing Services, UK).

Spheroid analysis. hTERT-RPE1 cells (American Type Culture Collection; CRL-4000) were seeded (2×10^5 cells per well in 6-well plates). Each stealth RNA (100 pmol) of Opti-Mem medium (Life Technologies) was transfected using Lipofectamine RNAi Max (Life Technologies) followed by incubation for 24 h at 37 °C. Trypsin treatment was used to collect RNAi-transfected cells from wells which were resuspended in 2 ml of 10% FBS (Hyclone, ThermoFisher Scientific)-DMEM. These resuspensions were seeded to 6 wells of a 12-well plate (Hydrocell, CellSeed Japan) and incubated for 48 h at 37 °C. Spheroids were fixed in 3% formalin and subjected to immunostaining. Reagents used for immunostaining: anti-β-catenin (BD transduction, 610154, 1:200), anti-FN (Sigma F3648, 1:500), Alexa Fluor 546 Phalloidin (Invitrogen, A22283,1:200). For the list of primers see Supplementary Table 5.

Western blotting. Spheroids were lysed in lysis buffer (0.5% TritonX-100, 150 mM NaCl, 20 mM Tris-HCl pH 7.5). The lysates were sheared with a 21-gauge needle, incubated on ice for 30 min and clarified by centrifugation at 20,817*g* for 15 min at 4 °C. The extracted proteins were separated by SDS–PAGE and transferred to immobilon transfer membrane (Millipore) for western blotting analyses. The primary antibodies were anti-YAP1 pAb (4912 Cell Signaling, 1:500), anti-fibronectin pAb (F3648, Sigma Aldrich, 1:1,000), anti-ARHGAP18 pAb (1:10,000)[17,21], anti-MYH9 pAb (3403 Cell Signaling, 1:1,000), anti-Phospho Ser1943-MYH9 pAb (5026 Cell Signaling, 1:1,000), anti-MYH10 mAb (8824 Cell Signaling, 1:1,000), anti-Phospho-Ser19 MLC2 (3675, Cell Signaling, 1:100), and anti-GAPDH mAb (sc32233, Santa Cruz, 1:5,000).

Actomyosin tension measurement by laser cutting. Laser cutting experiments were carried out using a UV-laser ablation system as previously described[17]. Tg(*actb2:myl12.1-eGFP*)[32] embryos were mounted in 1% low melting point agarose (Invitrogen) embedded in E3 medium inside a glass bottom Petri dish (Mattek). A 63× water immersion objective (NA = 1.2, Zeiss) was used to visualize the YSL actomyosin ring at respective epiboly stages. Cuts were made at a distance of 20 μm from the EVL/YSL boundary by applying 25 UV pulses at 1 kHz to 40 equidistant sites along a 20-μm-long line perpendicular to the EVL margin as depicted in Fig. 2e. Fluorescent images of embryos were captured using an iXon DU-897-BV camera (Andor Technology) with a 380 ms exposure time and 500 ms frame rate (LabVIEW v10.0.1). The ablation procedure itself took 1.2 s during which no images were acquired. Temperature was kept constant at 28.5 ± 1 °C throughout the experiment by means of a custom-built temperature chamber and an objective heating ring. The recoil velocity of the cortex in response to the cut opening was analysed using customized Matlab (v7.12) scripts based on particle image velocimetry (PIV) as previously described[17,38]. The component of the PIV flow field that is orthogonal to the cut line was averaged in two adjacent rectangles (Fig. 2f) for time frames up to 9 s post-ablation. The resulting recoil velocity curves for single embryo ablation experiments were averaged to yield the mean temporal recoil velocity curve for the depicted conditions (Fig. 2g). Laser ablation experiments that caused wound response recognizable by a strong accumulation of myosin following the ablation were discarded from the analysis. In these experiments leakage of yolk cytoplasm through a membrane opening may interfere with the cortical tension measurements[17].

Micropipette aspiration analysis. The whole neural tube was dissected out from st. 22 medaka embryos and was cut using a tungsten needle at the level of diencephalon-midbrain boundary. The micropipette was connected to a Microfluidic Flow Control System (Fluigent, Fluiwell) which was controlled via a custom-programmed Labview (National Instruments) interface. In the BSS medium, the neural tube was aspirated from the open end by a micropipette (internal radius = 30–35 μm) at a constant pressure ($\Delta P \approx 4.5$ mbar) for 10 min. Aspiration was imaged at 500 ms intervals by a Leica SP5 inverted confocal microscope using a Leica 20×, 0.7 NA objective. Temperature in the dish was kept constant at 28 °C by a heated sample holder. Measuring the tongue length of the tissue within the micropipette using FIJI software over time yielded the characteristic tissue flow curves during aspiration for WT and *hir* mutant neural tube explants. To reduce cortical tension WT neural tube explants were treated with ROCK inhibitor Y27632 (250 μM dissolved in water) for 15 min before performing the micropipette aspiration experiment.

Oligo DNA microarray analysis. For the Oligo DNA microarray analysis, total RNA samples were collected from hTERT-RPE1 multicellular spheroids. 3D-Gene Human Oligo chip 25k (TORAY) was used. Total RNA of YAP siRNA-transfected spheroids and that of negative control siRNA were labelled with Cy3 or Cy5 using the Amino Allyl MessageAMP II aRNA Amplification Kit (Life Technologies), respectively. The Cy3- or Cy5-labelled aRNA pools and hybridization buffer were mixed, and hybridized for 16 h at 37 °C. The hybridization was performed using

the supplier's protocols (http://www.3d-gene.com). Hybridization signals were scanned using a 3D-Gene Scanner 3000 (TORAY). Detected signals for each gene were normalized by a global normalization method (Cy3/Cy5 ratio median = 1). Genes with Cy3/Cy5 normalized ratios greater than 2.0 or less than 0.5 were defined, respectively, as commonly up- or downregulated genes. The results were deposited at GEO under the accession number GSE54146.

Quantitative RT–PCR analysis. Total RNA was isolated from WT and *hir* mutant embryos at various developmental stages using TRIzol (Invitrogen) according to the manufacturer's instructions. First-strand cDNA was synthesized from 1 μg total RNA using Superscript III reverse transcriptase (Invitrogen) with an oligo-dT primer. Each quantitative real-time RT–PCR was performed using the CFX96 real-time PCR detection system (Bio-Rad). Primers used for RT–PCR analysis are shown in Supplementary Table 5. For a 10 μl PCR, cDNA template was mixed with the primers to final concentrations of 250 nM and 5 μl of SsoFast EvaGreen Supermix (Bio-Rad), respectively. The reaction was first incubated at 95 °C for 3.5 min, followed by 45 cycles at 95 °C for 30 s, 65 °C for 30 s and 72 °C for 30 s.

Phylogenetic analysis of ARHGAP18-related genes in 11 metazoan species. Lists of homologues of ARHGAP18 family (TF314044) and its closely related families ARHGAP6 (TF316710) and ARHGAP11 (TF332212) in 11 metazoan model species were downloaded from the Treefam database. Amino-acid sequences for these genes were downloaded from Ensembl. Multiple sequence alignment was performed using the PRANK package. This alignment was used to infer the phylogenetic relationship of these genes using maximum likelihood using FastTree 2.1.

ARHGAP siRNA screening in HeLa cell line. A library of siRNAs targeting human GAPs was obtained from Invitrogen. HeLa cells cultured in 24-well plates were transfected with siRNAs (20 nM) using Lipofectamine RNAiMAX. After 72 h, cells were fixed with 4% PFA and stained with FITC-labelled phalloidin (Invitrogen). Images were taken using an Olympus IX71 fluorescence microscope.

Statistical analyses. Statistical significance between WT and mutant groups was tested using independent two-tailed *t*-tests (for two-way comparisons) and one-way ANOVAs (for multiple comparisons), with a Dunnett's T3 post-hoc where necessary, in SPSS 20 (IBM) or Prism v5.0 (GraphPad). The Dunnett's T3 post-hoc assumes variances to be unequal and allows comparisons of groups with different *n* numbers. To test for differences in mitotic orientation between WT and *hir* we performed the Kolmogorov–Smirnov (KS) test (http://www.physics.csbsju.edu/stats/KS-test.n.plot_form.html). The KS test makes no assumptions about the distribution of data being tested. Sample size was not pre-determined. We repeated experiments a minimum of three times with sufficient *n* numbers for each repeat to be confident that reported results are representative. Randomization was not applied to allocate embryos to experimental groups. Blinding to group allocation was not used. Error bars on graphs show ± standard error of the means (s.e.m.), except when stated otherwise. Data points that deviated by more than ± 3× the standard deviation of the sample mean were excluded from analysis.

***P* values and sample sizes.** *P*-values vs WT unless specified. Fig. 1c: $n_{cont} = 39$, $n_{hir} = 25$ ($P = < 0.001$), $n_{mYAPKDhir} = 24$ ($P = < 0.001$), $n_{mYAPKDhir+YAPmRNA} = 22$ ($P = 1.000$). Fig. 2b: $n_{WT} = 26$, $n_{hir} = 14$ ($P = 0.0001$). Fig. 4b: $n_{contsiRNA} = 7$, $n_{YAPsiRNA} = 5$ ($P = 0.023$). Extended Data Fig. 2h: $n_{contMO} = 20$, $n_{ZFYAPTBMO} = 11$ ($P = < 0.001$), $n_{ZFYAP;TAZTB} = 10$ ($P = < 0.001$). Extended Data Fig. 2i: n_{WT} st. 20 = 5, st. 22 = 8, st. 24 = 13, st. 26 = 6, st. 28 = 10, n_{hir} st. 20 = 8, st. 22 = 4, st. 24 = 6, st. 26 = 9 ($P = 0.0284$), st. 28 = 5 ($P = 0.0088$), n_{TAZMO} st. 20 = 5, st. 22 = 5, st. 24 = 10, st. 26 = 12, st. 28 = 12. Extended Data Fig. 2j: n_{WT} st. 20 = 11, st. 22 = 7, st. 24 = 10, st. 26 = 11, st. 28 = 11, n_{hir} st. 20 = 7, st. 22 = 7, st. 24 = 11, st. 26 = 13 ($P = 0.0158$ vs TAZMO st. 26), st. 28 = 7 ($P = 0.0075$ vs TAZMO st. 28), n_{TAZMO} st. 20 = 5, st. 22 = 5, st. 24 = 10 ($P = 0.0007$), st. 26 = 8 ($P = 0.0008$), st. 28 = 6 ($P = 0.0120$). Extended Data Fig. 3b: $n_{WT} = 174$, $n_{hir} = 70$ ($P = < 0.001$), $n_{mYAPKDhir} = 85$ ($P = < 0.001$), $n_{MRLCAA > WT} = 135$ ($P = < 0.001$), $n_{MRLCDD>hir} = 92$ ($P = 0.1830$ vs *hir*). Extended Data Fig. 4b: $n_{WT} = 3$, $n_{hir} = 3$. Extended Data Fig. 5b: n_{WT} cell stacking = 9, cell slippage = 8, parallel division = 5, n_{hir} cell stacking = 3 ($P = <0.01$), cell slippage = 21 ($P = <0.05$), parallel division = 5. Extended Data Fig. 5d: KS-test, $P = 0.01$, n_{WT} st. 22–24 = 32, st. 25–26 = 13, n_{hir} st. 22–24 = 14, st. 25–26 = 20. Extended Data Fig. 6b: $n_{WT} = 10$, $n_{70kDaFN>WT} = 13$ ($P = 0.0032$), $n_{hir} = 6$ ($P = 0.0001$), $n_{YAPS87A>hir} = 10$ ($P = 0.0013$ vs *hir*).

31. Porazinski, S. R., Wang, H. & Furutani-Seiki, M. Essential techniques for introducing medaka to a zebrafish laboratory–towards the combined use of medaka and zebrafish for further genetic dissection of the function of the vertebrate genome. *Methods Mol. Biol.* **770,** 211–241 (2011).
32. Maître, J.-L. *et al.* Adhesion functions in cell sorting by mechanically coupling the cortices of adhering cells. *Science* **338,** 253–256 (2012).
33. Hirose, Y. Varga, Z. M., Kondoh, H. & Furutani-Seiki, M. Single cell lineage and regionalization of cell populations during Medaka neurulation. *Development* **131,** 2553–2563 (2004).
34. Iwanami, N. *et al.* WDR55 is a nucleolar modulator of ribosomal RNA synthesis, cell cycle progression, and teleost organ development. *PLoS Genet.* **4,** e1000171 (2008).
35. Naruse, K. *et al.* A medaka gene map: the trace of ancestral vertebrate proto-chromosomes revealed by comparative gene mapping. *Genome Res.* **14,** 820–828 (2004).
36. Itoh, M., Nagafuchi, A., Moroi, S. & Tsukita, S. Involvement of ZO-1 in cadherin-based cell adhesion through its direct binding to alpha catenin and actin filaments. *J. Cell Biol.* **138,** 181–192 (1997).
37. Alexandre, P., Reugels, A. M., Barker, D., Blanc, E. & Clarke, J. D. Neurons derive from the more apical daughter in asymmetric divisions in the zebrafish neural tube. *Nature Neurosci.* **13,** 673–679 (2010).
38. Mayer, M., Depken, M., Bois, J. S., Jülicher, F. & Grill, S. W. Anisotropies in cortical tension reveal the physical basis of polarizing cortical flows. *Nature* **467,** 617–621 (2010).

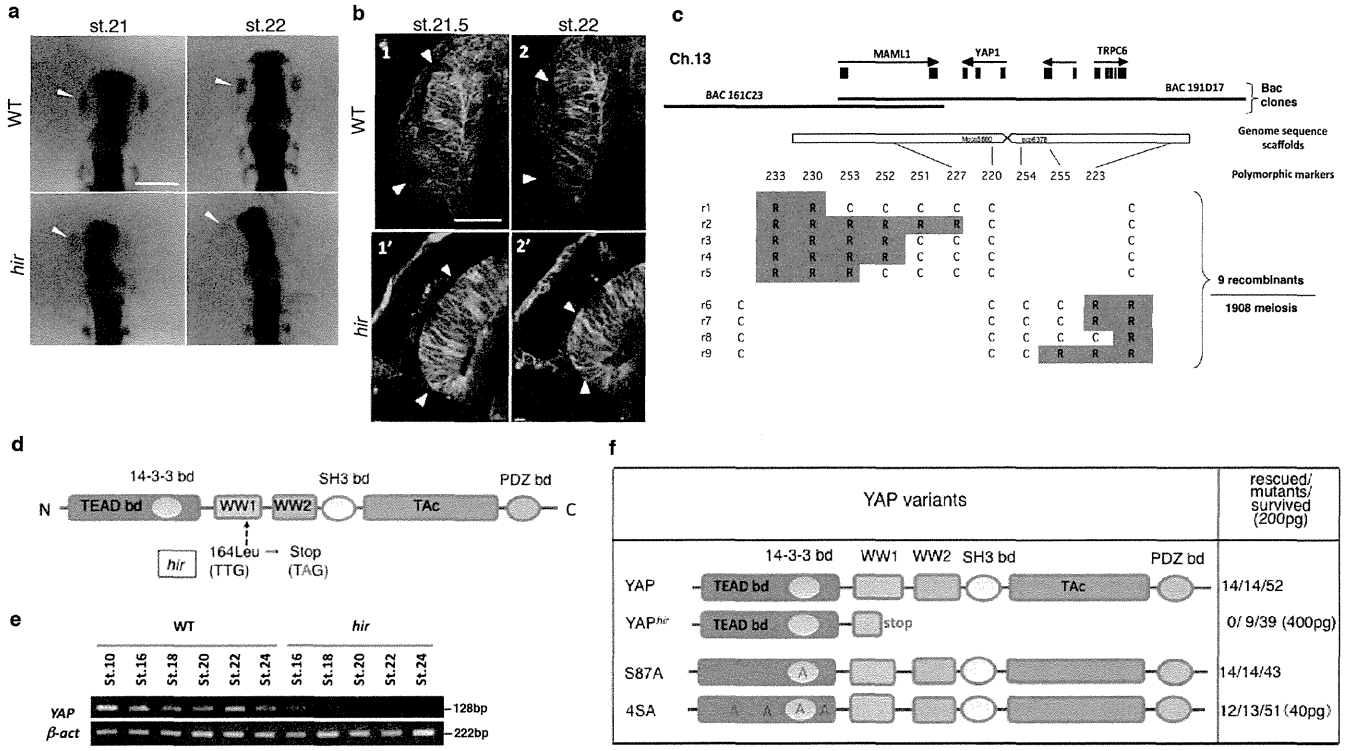

Extended Data Figure 1 | YAP is mutated in *hir* mutants. **a**, *In situ* hybridization of *sox3* showed that the lens placode (arrowhead) is specified in *hir* mutant embryos ($n = 3$) at st. 21. At st. 22, the nascent lens invaginated in WT ($n = 21$), but not in *hir* mutant embryos ($n = 13$, arrowhead). **b**, Two frames from time-lapse imaging of retina of embryos injected with membrane EGFP and nuclear red fluorescent protein (MNFP) mRNAs. In WT ($n = 10$), the nascent lens invaginates from st. 21 (**b1**, margins of the lens indicated by arrowheads with retina to the right), whereas in *hir* ($n = 7$) the lens mostly detached from the retina (**b2′**, arrowheads show lens remnants attached to the retina). Scale bars, 80 μm in **a**; 30 μm in **b**. **c**, Nine recombinants in 1,908 meiosis mapped *hir* close to the YAP gene on chromosome 13 (R: recombinant, C: non-recombinant embryos). **d**, YAP cDNA encodes six protein binding domains/motifs and one transcription activation (TAc) domain; a non-sense mutation in WW1 domain in *hir*. **e**, RT–PCR analysis of YAP mRNA during development. *β-actin* as control. **f**, mRNA of normal YAP and its variants were injected into *hir* mutants. The numbers represent: *hir* phenotype rescue judged via brain thickness, heart migration and Cuvier's duct formation; mutants (judged by genotyping when necessary); survived injected embryos of $hir^{+/-}$ crosses. High dose (400 pg) mRNA of YAP^{hir} variant was injected into WT embryos to examine dominant-negative effects. The rescue by YAP^{4SA} variant required only 20% of the amount required to rescue using normal *YAP* mRNA.

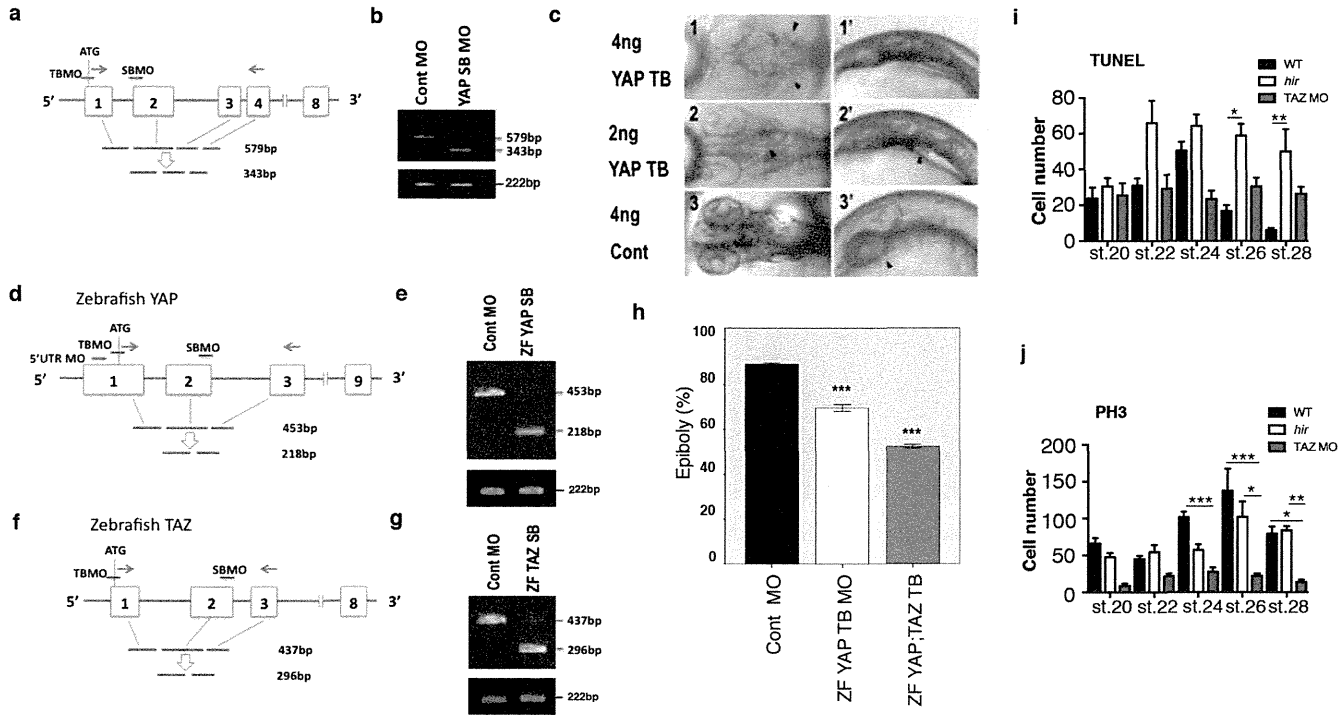

Extended Data Figure 2 | Morpholino knockdown in medaka and zebrafish. **a**, Design of medaka YAP TB and SB MOs relative to translation start (ATG), exons (numbered boxes) and introns. Primers (arrows) used to assess the efficiency of SB MO KD. **b**, Upper panel, proper splicing of YAP transcripts (579 bp) was nearly fully blocked (343 bp, <5% of normal level) by YAP SB MO (5 ng), assessed by RT–PCR; lower panel, *β-actin* control. **c**, WT embryos injected with YAP TB MO and standard control MO. **c1**–**c3** Dorsal and **c1′**–**c3′** lateral views (also Supplementary Table 1). Arrowheads indicate location of heart progenitors. Body flattening and bilateral cardiac progenitor cell migration was affected in a dose-dependent manner. **c2**, **c2′**, Bilateral cardiac progenitor cells fused at the midline but did not migrate anteriorly; **c1**, **c1′** their migration arrests next to the ears at the high dose. The two distinct YAP morpholinos (YAP TB and SB MOs) mimicked the *hir* phenotype (*hir* mutants have a *cardia bifida* phenotype (arrowheads in Fig. 1a1 and a1′)) in a dose-dependent manner. To further verify specificity of the YAP MOs, YAP TB MO was co-injected with human YAP mRNA that does not hybridize with the YAP TB MO. Injection of YAP TB (but not YAP SB) MO into *hir* mutant embryos enhanced the blastopore closure phenotype of *hir* mutants (Fig. 1b, c, Supplementary Table 2). These maternal YAP KD *hir* mutant embryos failed to close the blastopore. Less than half the amount (2 ng) of YAP TB MO was required for causing this phenotype in *hir* mutants compared to that required for WT embryos (5 ng). This blastopore closure phenotype was rescued by medaka YAP mRNA (200 pg) co-injection. **d**–**g**, Zebrafish (ZF) WT embryos injected with three distinct ZFYAP MOs (TB, 5′ UTR and SB) exhibit the blastopore closure phenotype as in medaka (Supplementary Table 3). Efficiencies of ZF YAP and TAZ SB MO KD (1.5 ng each) were assessed by RT–PCR using primers in **d**, **f**, respectively as in **a**, **b**. As reported by Gee *et al.*, co-injection of ZF YAP mRNAs did not rescue the ZF YAP MO phenotype in zebrafish[11]. **h**, Co-injection of ZF TAZ MO (total 2 ng) enhanced slow epiboly of YAP TB KD-injected embryos; control = 89 ± 4.16% ($n = 20$), YAP KD = 70.09 ± 4.7% ($n = 11$), YAP/TAZ KD = 52.5 ± 2.64% ($n = 10$). Error bars show ± s.e.m. $^{***}P < 0.001$, one-way ANOVA. *y* axis shows percentage epiboly. **i**, **j**, TUNEL for cell death and phosphohistone H3 (PH3) antibody staining for cell proliferation (see methods for sample sizes). Stained cells in the neural tube were counted. Error bars indicate ± s.e.m. $^{*}P < 0.05$, $^{**}P < 0.01$, $^{***}P < 0.001$, one-way ANOVA.

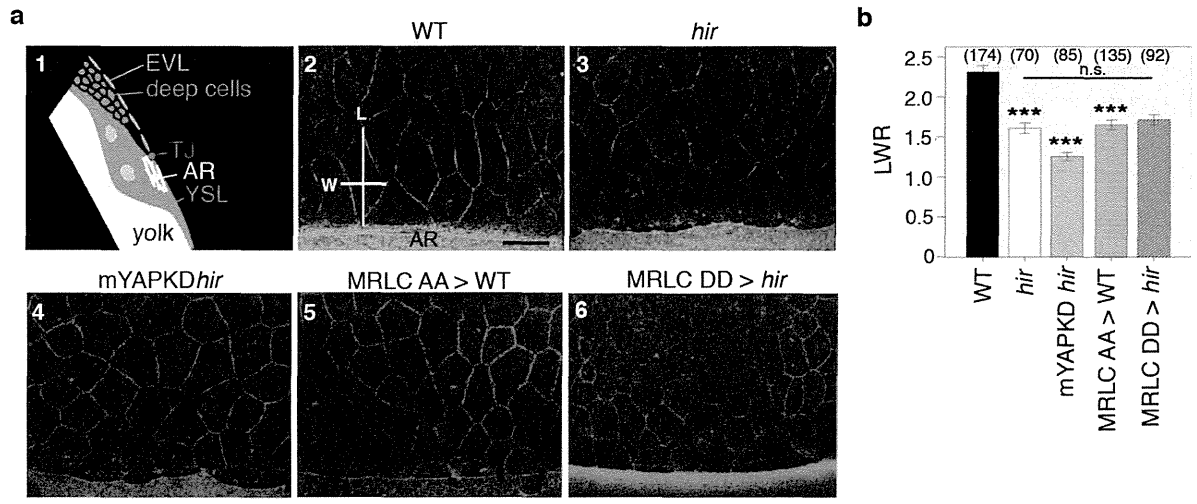

Extended Data Figure 3 | Anisotropic enveloping layer cell shape analysis in *hir* mutants. **a1**, Schematic of sectional view of blastoderm margin of a gastrulating embryo (TJ, tight junction; AR actomyosin ring; YSL, yolk syncytial layer; EVL, enveloping layer); **a2–a6**, EVL shape was visualized in phalloidin-stained fixed medaka embryos at 75% epiboly (st. 16, 21 hpf) and compared among, 2 WT ($n = 14$); 3 *hir* ($n = 9$); 4 maternal YAP KD *hir* mutants (mYAPKD*hir*) by TB MO-injection into *hir* embryos ($n = 12$), 5 MRLC-AA (dominant negative form) mRNA-injected WT ($n = 6$); and 6, MRLC-DD (constitutive active form) mRNA-injected *hir* embryos ($n = 4$). **b**, EVL shape anisotropy quantification by the length/width ratio (LWR, shown in **a2**) of marginal EVL cells (up to 4 rows back from the EVL/YSL boundary, shown in Fig. 2d bracket). While EVL shape anisotropy was reduced in *hir* mutant embryos (**a3**) to a level comparable to that of MRLC blocked embryos (**a5**), activation of MRLC in *hir* (**a6**) did not rescue it. Parentheses indicate number of cells measured. Scale bar 30 μm. Error bars represent ± s.e.m. ***$P < 0.001$, one-way ANOVA.